Journal Pre-proofs

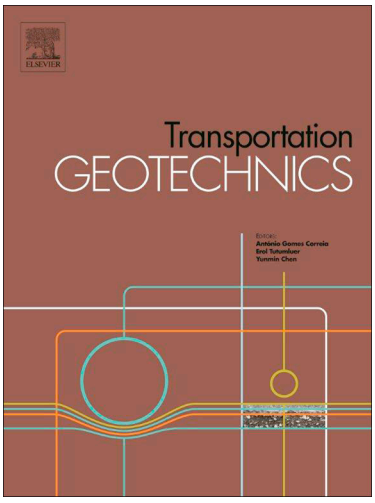

Original Article

Airport infrastructure risk to liquefaction by deploying multi-modal data and remote sensing

Maria Taftsoglou, George Papathanassiou, Sotirios Valkaniotis, Sotirios Argyroudis, Stergios-Aristoteles Mitoulis

PII: S2214-3912(25)00368-X
DOI: https://doi.org/10.1016/j.trgeo.2025.101849
Reference: TRGEO 101849

To appear in: *Transportation Geotechnics*

Received Date: 6 September 2025
Revised Date: 6 December 2025
Accepted Date: 11 December 2025

Please cite this article as: M. Taftsoglou, G. Papathanassiou, S. Valkaniotis, S. Argyroudis, S-A. Mitoulis, Airport infrastructure risk to liquefaction by deploying multi-modal data and remote sensing, *Transportation Geotechnics* (2025), doi: https://doi.org/10.1016/j.trgeo.2025.101849

Airport infrastructure risk to liquefaction by deploying multi-modal data and remote sensing

Maria Taftsoglou

Department of Civil Engineering, Democritus University of Thrace, Xanthi, Greece

George Papathanassiou, Sotirios Valkaniotis

Department of Geology, Aristotle University of Thessaloniki, Thessaloniki, Greece

Sotirios Argyroudis

Department of Civil and Environmental Engineering, Brunel University of London, Uxbridge, UK

& www.MetaInfrastructure.org

Stergios-Aristoteles Mitoulis

The Bartlett School of Sustainable Construction, University College London, UK

& www.MetaInfrastructure.org

ABSTRACT

Airports are critical components of transport infrastructure, contributing to regional socioeconomic vitality and serving as key hubs for emergency response during natural disasters. However, their operations are highly vulnerable to geohazards such as earthquake-induced soil liquefaction and associated ground failures. Despite this vulnerability, there is currently a lack of rapid, regionally scalable tools for assessing liquefaction-related risks specific to airport infrastructure. This paper for the first time in the literature addresses this gap by introducing a practical, geomorphology-informed methodology for the preliminary identification of liquefaction-prone areas and the rapid assessment of risk to airport infrastructure. The proposed approach leverages multimodal data, including surface geological mapping, tailored remote sensing inputs, and established seismic risk models, to develop liquefaction susceptibility maps and estimate potential damage. The methodology is applied to a real-world airport case study under a representative seismic scenario, revealing that large sections of the runway and taxiways are situated on highly susceptible soils. The HAZUS methodology is employed to assess potential losses and is validated using data from three international airports that have experienced documented liquefaction-related damage. This

study provides a novel, scalable, and cost-effective framework that can be applied globally to support airport operators, risk engineers, and insurers in rapidly identifying vulnerable zones, prioritizing inspections, and developing targeted mitigation strategies. It contributes to advancing geotechnical risk assessment by bridging regional-scale mapping with infrastructure-specific vulnerability analysis. The methodology has the potential to be extended and applied to other critical infrastructure—such as ports, highways, railways, and industrial facilities—located in areas susceptible to liquefaction.

Nomenclature

List of symbols

K_M: moment magnitude (M) correction factor

K_W: correction factor for groundwater depths (d_w) other than 5ft (1.52m)

P_{ml}: proportion of map unit susceptible to liquefaction

IM: Intensity Measure

M: moment magnitude

$P\,[Liquefaction_{sc}]$ or PLsc: probability of liquefaction

P (DS = ds | IM): Probability that the airport asset is in a specific damage state ds, conditional on the imposed intensity measure (IM).

$P\,[Liquefaction_{sc}\,|PGA = a|]$: conditional liquefaction probability for a given susceptibility category at a specified level of peak ground acceleration

Pf (DS≥ds|IM): Probability that the airport asset damage state DS meets or exceeds a specified damage threshold ds, conditional on the imposed intensity measure (IM). The damage states typically include: s/m (slight/minor), e (extensive), c (complete)

PGA: Peak Ground Acceleration

PGD: Permanent Ground Deformation

RR: Repair Ratio

V_{S30}: average shear-wave velocity in the upper 30 meters of the ground

CTI: compound topographic index

Introduction

Transport infrastructure is increasingly vulnerable to a broad spectrum of geohazards and climate-related impacts, which threaten its functionality, safety, and long-term sustainability. In addition to well-documented seismic risks, infrastructures such as airports face growing exposure to hazards exacerbated by climate change, including ground instability, subsidence, and extreme weather events. The interaction between physical hazards and infrastructure performance must be understood through integrated, spatially aware risk assessment frameworks to inform adaptive planning and resilience strategies (Yesudian and Dawson, 2021). Among geohazards, earthquakes remain a significant threat, particularly when compounded by secondary effects such as soil liquefaction and landslides. Liquefaction refers to the loss of soil strength and stiffness due to increased pore water pressure during seismic shaking, causing saturated, loose granular soils to behave like a fluid (Youd, 1973). This phenomenon is typically triggered in fluvial plains, coastal zones, and reclaimed lands with young, water-saturated sediments (Knudsen and Bott, 2011; Bastin et al., 2015, 2018; Papathanassiou et al., 2016; Minarelli et al., 2022; Valkaniotis et al., 2024). The resulting ground deformation—settlement, lateral spreading, and foundation failure—can inflict extensive damage on critical infrastructure systems, including airports.

As functionally critical and spatially constrained components of the transport network, airports are particularly susceptible to geohazards—especially soil liquefaction—due to their frequent location in low-lying, reclaimed, or alluvial terrain. Runways, taxiways, and critical support systems (e.g. control towers, fuel pipelines, and communication infrastructure) require flat, open land, which often coincides with regions characterised by loose, saturated soils. These conditions, when combined with seismic activity, create a high risk for liquefaction-induced ground failure (Geyin and Maurer, 2020; Ramos et al., 2020; Tan et al., 2018). Beyond their operational sensitivity, the societal and economic importance of airports for tourism and trade, they are vital hubs for emergency response and humanitarian aid, enabling the rapid mobilisation of resources and evacuation of affected populations following natural (e.g. earthquakes) or human induced disasters (e.g. conflicts). According to the Airport Council International (ACI; Adler et al., 2024), European airports alone support 14 million jobs and contribute €851 billion to GDP—approximately 5% of the continent's total economic output. Given these critical functions, understanding and mitigating liquefaction risk in airport environments is essential.

Historical earthquake events have demonstrated the diverse and often severe impacts of liquefaction on airport infrastructure, ranging from pavement cracking and settlement to control tower and utility failures. For instance, during the 1989 Loma Prieta earthquake (USA), the main runway of Oakland International Airport experienced extensive liquefaction, including sand boils and lateral spreading (Seed et al., 1991; H.T Harvey & Associates, 1993; Holzer, 1998), with repair costs estimated at $5.7 million (Metropolitan Transportation Commission, 2011). Similar effects were observed at Alameda Naval Air Station, forcing runway closures for up to three months (EERI, 1990). The 1994 Northridge earthquake (USA) damaged the control tower at Van Nuys Airport (Schiff, 1995), while the 1995 M_w 6.9 Kobe earthquake (Japan) caused surface cracks and structural impacts at Kansai and Itami Airports (EERI, 1995b). During the 2001 Nisqually earthquake (USA),

King County International Airport experienced extensive ground deformation and pavement cracking, with total repair and upgrade costs reaching $4.4 million (Bray et al., 2001). Most recently, the 2023 Türkiye-Syria earthquakes triggered severe liquefaction-induced damage at Hatay International Airport, particularly affecting the eastern runway (Taftsoglou et al., 2023). These examples underline the urgent need for proactive, regionally scalable methods to assess and mitigate airport vulnerability to liquefaction.

Over recent decades, multiple methodologies have been developed to evaluate liquefaction potential and its impacts on infrastructure. Widely used approaches include the Liquefaction Potential Index (LPI) and Liquefaction Severity Number (LSN), which assess liquefaction risk based on in-situ test data such as the Standard Penetration Test (SPT) and Cone Penetration Test (CPT) (Iwasaki et al., 1982; Papathanassiou, 2008; van Ballegooy et al., 2012; Maurer et al., 2014). Complementary tools such as HAZUS, SYNER-G, and REDARS 2 (Werner et al., 2006; Pitilakis et al., 2014; D'Apuzzo et al., 2020; FEMA, 2022) provide standardised frameworks for assessing liquefaction risk for transportation systems. Nonetheless, accurate site-specific vulnerability assessments require detailed geotechnical testing, which can be costly and time-consuming. Laboratory analyses (e.g. grain size distribution, Atterberg limits) and in-situ methods are necessary to estimate safety factors and determine the liquefaction potential of each soil layer (Youd et al., 2001; Cetin et al., 2004; Boulanger and Idriss, 2014). Moreover, they provide essential parameters for the development and calibration of numerical models (Finn, UBC Sand, PM4Sand, SANISAND etc.), allowing the simulation of the soil response during liquefaction (Byrne et al. 1991; Beauty et al., 1998; Dafalias and Manzari, 2004; Boulanger and Ziotopoulou, 2017; Ecemis, 2021; Zhang et al., 2024) and consequently the estimation of the potential for vertical or later ground displacement and structural damage under various earthquake scenarios (Zalachoris et al., 2021).

This renders such evaluations impractical for large-scale or time-sensitive applications. At the regional level, susceptibility assessment relies on geomorphological indicators such as sediment age, depositional environment, and groundwater depth. Established frameworks for regional-scale mapping include the methodologies of Youd and Perkins (1978), Wakamatsu (1992), CDMG (1999), and Witter et al. (2006). However, these methods are often hindered by the limited availability or insufficient resolution of geomorphological data.

Remote sensing technologies address these limitations by providing multi-temporal observations of the surficial geological environment. Particularly, optical satellite imagery allows the identification of variations in soil color and moisture, facilitating the detection not only of areas affected by liquefaction phenomena but also of the different geomorphological features, in which such occurrences are observed. In addition, radar-based remote sensing techniques, such as InSAR and LiDAR, have proven very useful in monitoring post-seismic ground deformation over large areas (Barnhart et al., 2018; Albano et al., 2024). For instance, employing a combination of very high-resolution optical satellite imagery and InSAR coherence analysis, Taftsoglou et al. (2023) identified liquefaction phenomena in the eastern runway of Hatay International airport after the 2023 Türkiye-Syria earthquakes.

Despite their global economic significance—with an estimated total impact of $4.1 trillion (Air Transport Action Group – ATAG)—airports remain particularly vulnerable to seismic ground deformations, especially liquefaction. Given their dual role in economic connectivity and emergency response, ensuring their resilience is vital. This study introduces a novel, scalable, and data-efficient methodology for assessing liquefaction-related risk to airport infrastructure at a regional scale, addressing the need for rapid, transferable tools in seismic risk management.

The proposed approach integrates remote sensing, geomorphological mapping, and scenario-based seismic modelling to generate susceptibility classifications, estimate liquefaction probability, compute permanent ground deformation (PGD), and evaluate potential economic losses—all without requiring detailed site-specific investigations. The methodology is demonstrated using Kavala International Airport (KVA) in North Greece as a representative case study. The method is further validated using historical case studies from three international airports affected by liquefaction. By bridging regional geomorphic classification with infrastructure-specific risk estimation, this research offers a generalisable framework to support airport operators, risk engineers, and policymakers in identifying vulnerable assets and developing targeted mitigation strategies (Lakkimsetti and Latha, 2023; Amanta and Dasaka, 2021).

Methodology

The proposed methodology is structured into two main phases comprising a total of nine steps. **Phase I** follows a workflow adapted from Taftsoglou et al. (2022) and focuses on assessing the liquefaction susceptibility of the study area through the following three steps: (1) data collection and processing, (2) mapping geomorphological features, (3) classification of susceptible geological units, and liquefaction susceptibility mapping. **Phase II** is dedicated to evaluating the risk to critical infrastructure within the same region. It comprises an additional five steps: (4) collection of airport infrastructure data, (5) estimation of liquefaction probability, (6) estimation of permanent ground displacement (PGD), (8) vulnerability and loss assessment, and (9) risk assessment. The overall workflow is illustrated in Figure 1.

Phase I: Assessment of liquefaction susceptibility

Step 1 – Data collection and processing. This phase begins with the acquisition and preparation of geospatial datasets at a regional scale (see Step 1 in Figure 1). The resolution and quality of the resulting susceptibility map depend heavily on the availability and accuracy of geological and topographic data. To address potential data limitations, a combination of remote sensing sources and historical cartographic datasets is utilised, including:

- **Geological map sheets**: Serve as the primary data source for delineating Quaternary deposits, such as fluvial, floodplain and lagoonal. Nevertheless, due to their limited information concerning the geomorphological evolution of the deposits, remote sensing data are employed.

- **Historical aerial imagery**: Provides valuable insights into pre-modern surficial geomorphology. Imagery predating the 1950s is preferred to minimise distortions from anthropogenic alterations, though availability varies by location and is typically obtained from national or regional mapping authorities. Acquisition relies on image overlap, where common points identified in successive pairs are used for mosaicking and generating orthophoto maps of the study area.

- **High-resolution (<5 m) digital elevation models (DEMs)**: Derived from stereo aerial or satellite imagery or from airborne LiDAR surveys. These are instrumental in detecting subtle geomorphic features such as river levees and free-face areas prone to lateral spreading. Availability of LiDAR topographic surveys is limited but can be substituted by extracting a high-resolution digital surface model (DSM) from stereo very high resolution (VHR) optical satellite imagery such as WorldView, SPOT6/7 or Pleiades.

- **Declassified satellite imagery (e.g., Corona, Hexagon)**: Grayscale imagery from the 1960s–1970s that provides broader coverage than traditional aerial photographs. These datasets significantly reduce processing time by capturing larger areas, but they require orthorectification before analysis. Since images are taken at oblique angles and are subject to terrain-induced distortions, software such as ERDAS IMAGINE is typically used to project them onto a horizontal plane, enabling accurate georeferencing.

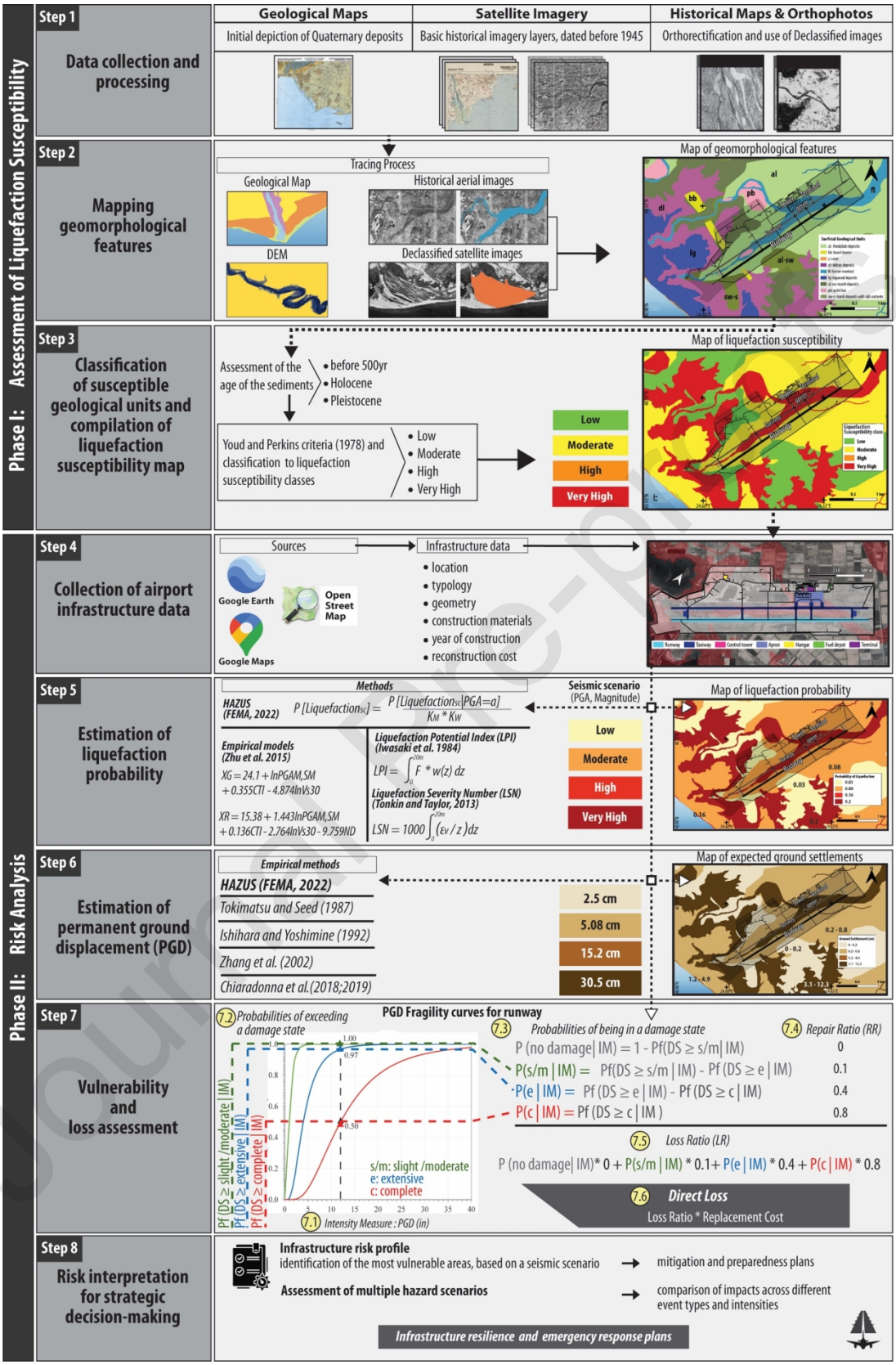

Figure 1: Methodology for assessing liquefaction risk for airport infrastructure by deploying multi-modal data and remote sensing.

- **Contemporary VHR satellite imagery and aerial orthophotos**: Although recent surface modifications may obscure some landforms, relict geomorphological features can often still be identified through variations in colour, wavelength signatures, and surface texture. Imagery acquired during periods of low vegetation cover or high surface moisture is particularly effective for this purpose. Such datasets are widely accessible through digital archives (e.g., Copernicus Data Library, ESA) or other repositories (e.g., SPOT World Heritage, ALOS AVNIR).

Following collection, these layers are imported into a GIS environment and analysed individually in relation to the geological and geomorphological formations they represent. The integration of these datasets enables the reconstruction of the area's geomorphological evolution and supports the production of a surficial geology map.

Step 2 – Mapping geomorphological features. In this step, geomorphological features are traced using multi-temporal and historical imagery. This enables identification of surficial units such as active and abandoned river channels, point bars, beach ridges, and coastal dunes—even in areas where these have been obscured by land development or the rapid evolution of the fluvial system, e.g. due to climate or human activity.

Specifically, beginning with the geologic map of the study area, the boundaries of the Quaternary sediments are delineated (Step 2.1 in Figure 2). These include fluvial, floodplain, and marsh deposits; Pleistocene deposits; as well as water bodies such as lagoons and the main river channel. Elevation transitions represented in the DEM (Step 2.2 in Figure 2) provide an accurate depiction of the boundaries between colluvial and floodplain sediments and also enable the identification of paleochannels and levees (both natural and anthropogenic) associated with the river course.

Historical aerial imagery (Step 2.3 in Figure 2) allows recognition of elements of the hydrographic network, such as abandoned channels and point bars. Point bars typically accumulate along the inner sides of meander bends and often display characteristic banding reflecting successive stages of growth. Dune deposits mapped along the coastal front show striations, while elongate sand ridges parallel to the shoreline represent beach-barrier formations. In a deltaic setting, aerial imagery assists in distinguishing deltaic deposits—appearing as brighter zones near river mouths—from lagoonal deposits, which are darker, as are marsh deposits situated within the floodplain interior.

Declassified satellite imagery (Step 2.4 in Figure 2) captures intermediate changes in surficial geology during the geomorphic evolution of the area. These datasets enable mapping of hydrographic changes such as channel desiccation, as well as progradation and erosion affecting deltaic and coastal deposits.

Finally, high- and very high-resolution satellite imagery (Step 2.5 in Figure 2) supports monitoring of modern landscape alterations, including infrastructure projects (e.g., transportation corridors, dams, airports). Their multispectral properties also facilitate the detection of relict geomorphic features, especially under low vegetation cover or high surface moisture.

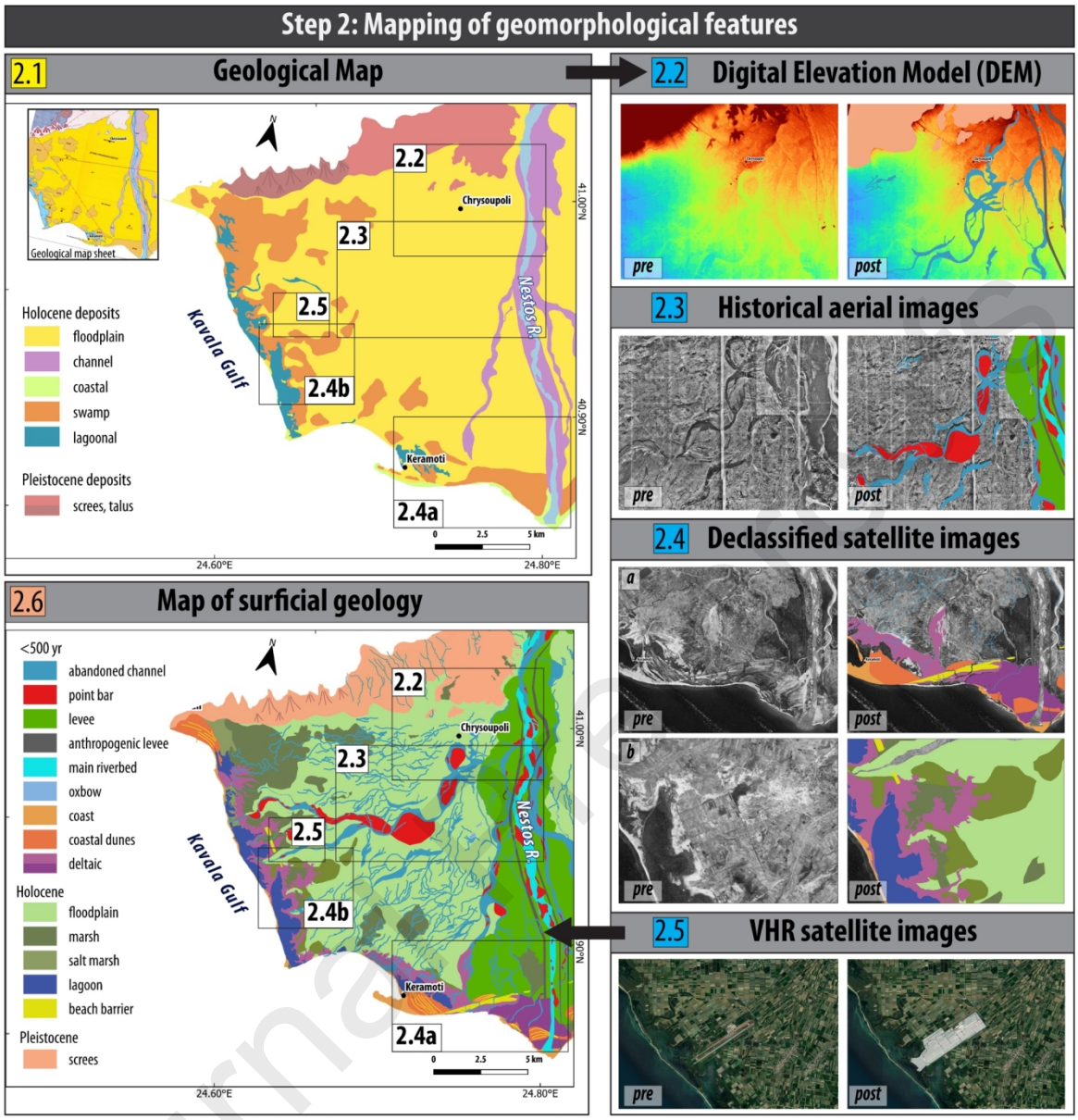

Figure 2: Mapping of geomorphological features, using (2.1) geological maps, (2.2) Digital Elevation Model (DEM), (2.3) historical aerial imagery, (2.4) declassified satellite data and (2.5) very high resolution (VHR) satellite imagery, followed by the compilation of a surficial geology map (2.6). The maps illustrate the western Nestos delta in northern Greece (modified after Taftsoglou et al. 2022). “Pre” and “Post” labels denote data before and after geomorphological feature mapping, respectively.

Step 3 – Classification of susceptible geological units and compilation of liquefaction susceptibility map. Geological and geomorphological maps are used to classify surficial units according to age (<500 years, Holocene, Pleistocene) and depositional environment. The assessment also considers relative surface modification, topographic position, and expert judgement. Liquefaction susceptibility is then determined following the criteria of Youd and Perkins (1978), which categorise the area into four classes: low, moderate, high, and very high susceptibility (see Step 3 in Figure 1).

Phase II: Risk analysis

Step 4 – Collection of airport infrastructure data. Before initiating the risk analysis, detailed information on the airport infrastructure is collected to support the subsequent vulnerability and loss assessment. This includes data on the location, typology, geometry, construction materials, year of construction, and estimated reconstruction costs for key assets such as runways, taxiways, aprons, terminal buildings, and control towers. Data sources include Google Earth, OpenStreetMap, and any available documentation such as procurement records, design specifications, structural drawings and maintenance reports. This data is organised into GIS layers, which allows for direct spatial integration with the liquefaction susceptibility map developed in Step 3. This geospatial alignment facilitates overlay analyses, ensuring that critical infrastructure elements can be accurately linked to their underlying geotechnical context. It also enables targeted estimation of PGD in Step 6, focusing specifically on the areas where airport facilities are located.

Step 5 – Estimation of liquefaction probability. With the susceptibility map from Phase I in place, this step estimates the probability of liquefaction under a defined seismic scenario. Several methods are available for this purpose:

- **Liquefaction Potential Index (LPI)** and **Liquefaction Severity Number (LSN)** (Iwasaki et al., 1978,1982; van Ballegooy et al., 2014): Having been applied in many studies (Toprak and Holzer, 2003; Papathanassiou, 2008; van Ballegooy et al., 2012; Maurer et al., 2015; Papathanassiou et al., 2015a) these indices integrate factors of safety for individual soil layers (up to 20 m depth) and are calculated based on in-situ test data such as SPT and CPT (Youd et al., 2001; Idriss and Boulanger, 2008; Boulanger and Idriss, 2014; Moss and Chen, 2008; Cetin et al., 2004).

- **Empirical models by Zhu et al. (2015)**: Utilise predictors such as the compound topographic index (CTI), the average shear-wave velocity in the upper 30 meters of the ground (V_{S30}), magnitude-scaled Peak Ground Acceleration (PGA_M) and PGA derived directly from ShakeMaps ($PGA_{SM)}$, surface moisture (SM), magnitude weighting factor (MWF), and distance from the coast (ND). These models offer both global (XG) and region-specific (XR) (coastal sedimentary basins) linear formulations for estimating liquefaction likelihood to assess the liquefaction likelihood.

- **Federal Emergency Managements Agency guidelines (FEMA, 2022)**: provide a simplified method, in which the likelihood of experiencing liquefaction at a specific location is primarily influenced by soil susceptibility, ground shaking amplitude and duration, and groundwater depth.

Given the study's objective for regional-scale rapid assessment, the HAZUS framework is adopted due to its efficiency and simplified data requirements. The probability of liquefaction is estimated using equation (1):

$$\mathrm{P}\left[\mathrm{Liquefaction_{sc}}\right] = \frac{\mathrm{P}\left[\mathrm{Liquefaction_{sc}}\,|\mathrm{PGA} = \mathrm{a}|\right]}{\mathrm{K_M} * \mathrm{K_W}} * \mathrm{P_{ml}} \qquad (1)$$

where:

- $\mathrm{P}\left[\mathrm{Liquefaction}_{\mathrm{sc}}\,|\mathrm{PGA}=\mathrm{a}|\right]$: is the conditional liquefaction probability for a given susceptibility category at a specified level of peak ground acceleration (PGA)
- $\mathrm{K_M}=0.0027\mathrm{M}^3-0.0267\mathrm{M}^2-0.2055\mathrm{M}+2.9188$: is the moment magnitude (M) correction factor
- $\mathrm{K_W}=0.022\mathrm{d_w}+0.93$: is the correction factor for groundwater depths ($\mathrm{d_w}$) other than 5ft (1.52m)
- $\mathrm{P_{ml}}$: proportion of map unit susceptible to liquefaction

Considering that for a given subsoil category, liquefaction is unlikely to occur over the whole portion of the geologic map, P_{ml} parameter is used to assess the probability of liquefaction at any given location. As the non-susceptible portions are expected to be smaller for higher susceptibilities, P_{ml} is inserted in order to quantify the proportion of geologic map unit deemed susceptible to liquefaction, i.e., the likelihood of susceptible conditions existing at any given location within the unit. Table 1 presents the default P_{ml} values based on regional studies.

Table 1 Proportion of map unit susceptible to liquefaction

Mapped Relative Susceptibility	Proportion of Map Unit (P_{ml})
Very High	0.25
High	0.20
Moderate	0.10
Low	0.05

Step 6 – Estimation of permanent ground displacement (PGD). To support the preliminary assessment of infrastructure damage, this step estimates liquefaction-induced ground settlement. Relationships from Tokimatsu and Seed (1987), Ishihara and Yoshimine (1992), and Zhang et al. (2002) can be used to correlate volumetric strain with relative density and factor of safety for clean sands. Moreover, laboratory cyclic shear tests on sands specimen, can demonstrate how combined shear and principal stress rotation contribute to settlement (Toyota and Takada, 2021). Although recent studies (e.g., Chiaradonna et al., 2018, 2019) recommend non-linear effective stress analyses in 1-D conditions for greater accuracy, such methods are data-intensive and less practical for regional-scale applications. Therefore, HAZUS approach is adopted here to estimate

PGD, by multiplying the probability of liquefaction (Step 5) by the representative settlement amplitude per susceptibility category (Table 2).

Table 2 Ground settlement amplitudes for liquefaction susceptibility categories

Relative susceptibility	Settlement (cm)
Very High	30.50
High	15.20
Moderate	5.08
Low	2.50
Very Low	0.00
None	0.00

Step 7 – Vulnerability and loss assessment. Fragility functions are used to estimate damage probabilities for a given intensity measure, such as PGD (Argyroudis, 2022; McKenna et el., 2021). Due to the limited availability of vulnerability models for airport infrastructure, the fragility functions from the HAZUS methodology are commonly adopted. These functions define the probabilities of exceeding specific damage states (slight, moderate, extensive, and complete) based on PGD values calculated in Step 6. To estimate expected losses, representative repair ratios—defined as the ratio of repair to replacement cost—are applied to each damage state. The average loss ratio is then calculated by weighting these repair ratios with the corresponding damage probabilities, allowing for the assessment of total expected loss under the selected seismic scenario.

Step 8 - Risk interpretation for strategic decision-making. The final step involves the integration of previous analytical outputs to generate a comprehensive risk profile for the airport under the selected seismic scenario. This profile supports the identification of the most vulnerable areas within the facility and informs prioritised decision-making for mitigation and preparedness planning. This step may also involve the assessment of multiple hazard scenarios, allowing stakeholders to compare impacts across different event types or intensities. By consolidating risk information into a unified framework, the process facilitates evidence-based strategies for enhancing infrastructure resilience, emergency response planning, and long-term investment decisions.

Case Study

Kavala International Airport (KVA) is situated on the western margin of the Nestos delta plain in Thrace, northern Greece. Constructed in the 1980s on recent Holocene deposits and located near active onshore and offshore fault systems, KVA is of particular interest for the analysis of liquefaction susceptibility and vulnerability of its units. This section demonstrates the implementation of the proposed methodology for assessing liquefaction susceptibility and associated risk, as outlined in the previous section.

Phase I – Liquefaction susceptibility assessment

In line with **Step 1**, geological map sheets at a scale of 1:50,000 (Hellenic Survey of Geology and Mineral Exploration – HSGME) were collected. Historical orthophoto maps dated prior to 1945 (Hellenic Cadastre) and declassified CORONA (KH-4) satellite imagery from 1960 and 1968 (USGS/NARA) were used to reconstruct the surficial landscape prior to extensive land modifications. These were complemented by VHR satellite imagery from Google Earth to assess current land cover conditions, and a digital surface model (DSM) with 5 m resolution (Hellenic Cadastre) to enhance the interpretation of subtle topographic features.

Initial review of the official geological maps, published by HSGME, indicated undivided alluvial and floodplain deposits across the area, with the airport itself situated on swamp and floodplain sediments of Holocene age. However, further interpretation using remote sensing, topographic data and historical imagery, as part of **Step 2**, enabled the delineation of geomorphological features previously obscured by anthropogenic alterations (Figure 3). The analysis revealed that KVA was largely constructed on former fluvial and deltaic deposits associated with a historic river network that was diverted and entrenched in 1952. The traced features included abandoned channels, point bars, beach barriers, floodplain and deltaic deposits, as well as marsh sediments. The resulting geomorphological map indicated that a significant portion of airport facilities, including parts of the runway, lie on the footprint of an abandoned river branch of old estuaries, while the remaining infrastructure spans floodplain and marshland formations (Figure 3, Figure 4).

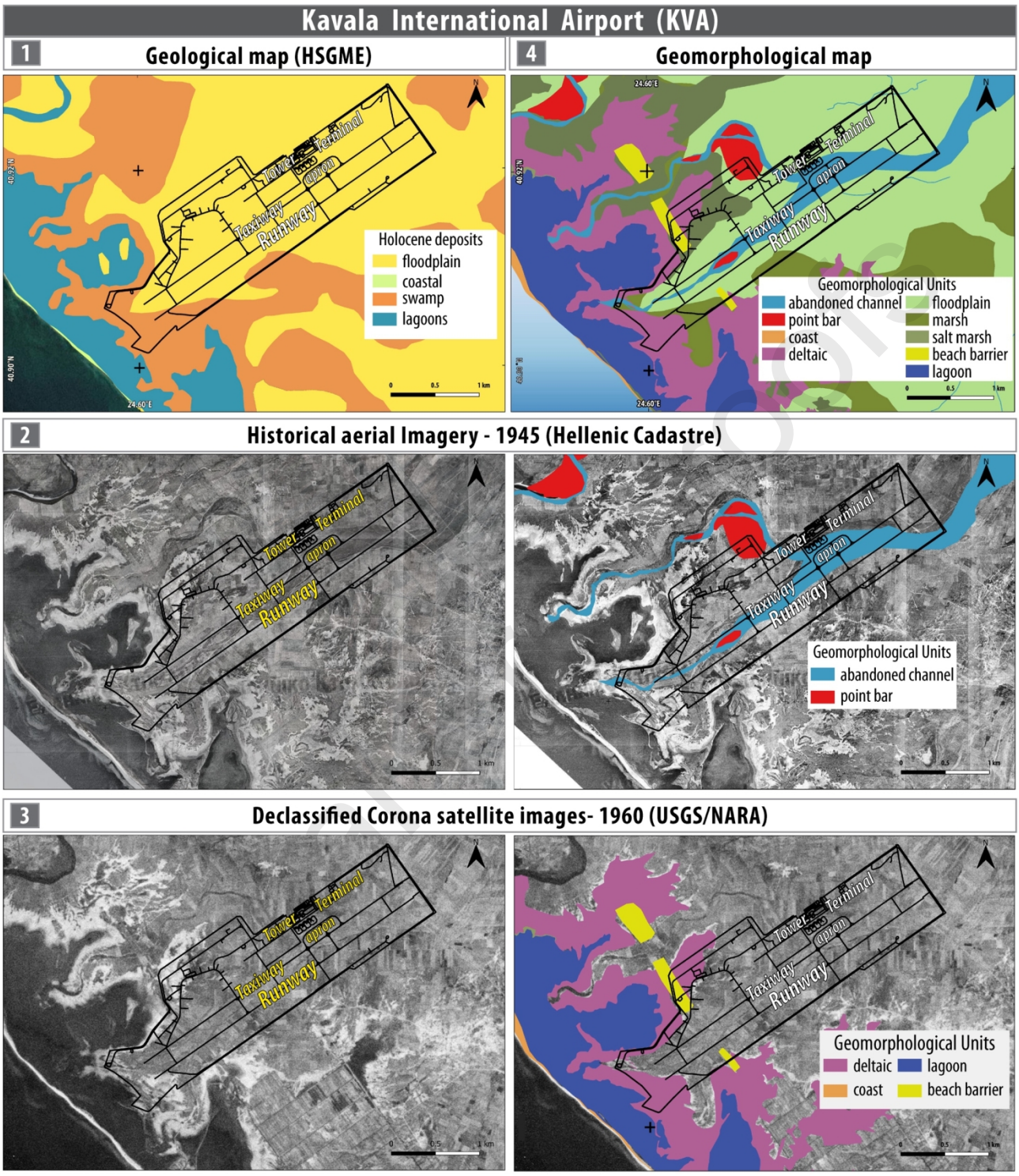

Figure 3: Use of of (1) geological map, (2) historical aerial images and (3) declassified satellite images for the compilation of the geomorphological map for KVA region (4).

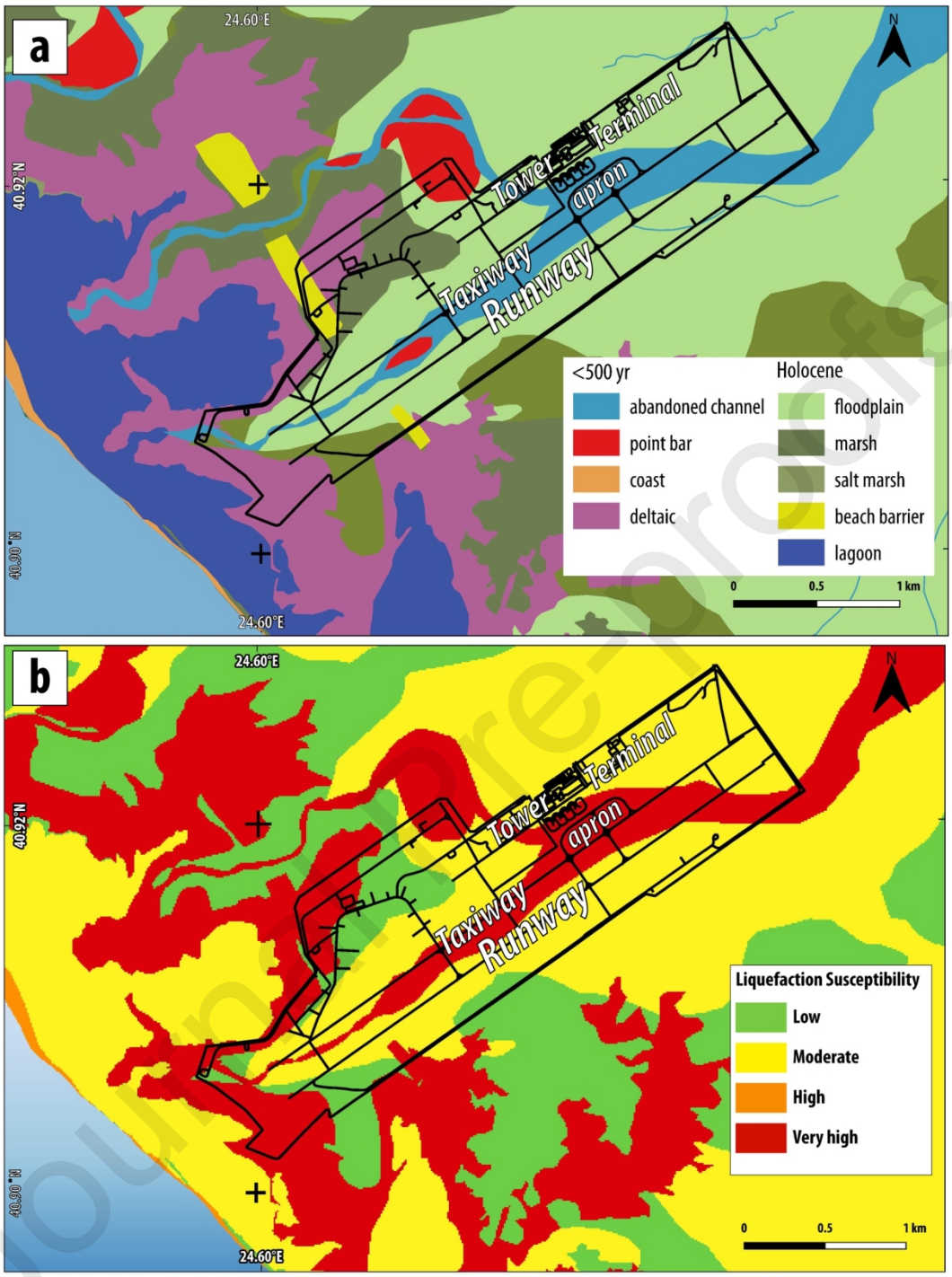

Figure 4: (a) The new geomorphological map of surficial geological units and (b) the liquefaction susceptibility map for the area of KVA.

In **Step 3**, sediment units were classified based on age (younger than 500 years, Holocene, and Pleistocene), and depositional environment. Using the Youd and Perkins (1978) criteria, the most susceptible units were identified as abandoned meanders, point bars, beach barriers, and deltaic deposits—primarily located in the central, northwestern, and southwestern parts of the airport. High susceptibility was also identified near the

coastal zone. Floodplain deposits, which dominate the area, were classified as moderately susceptible, while marsh deposits along the northeastern and southeastern margins were assigned low susceptibility. Based on this classification, a liquefaction susceptibility map was developed, categorising the airport site into zones of low, moderate, high, and very high susceptibility (Figure 4).

Phase II – Risk Analysis

In accordance with **Step 4,** a GIS-based map of the KVA airport infrastructure was developed using data sourced primarily from Google Maps (Figure 5). This map includes the location and spatial footprints of critical components such as runways, taxiways, aprons, and main buildings. The geospatial organisation of this information enabled direct overlay with the liquefaction susceptibility zones established in Step 3, ensuring spatial consistency across the analysis. For the purposes of the risk assessment, particular emphasis was placed on the runways, taxiways, and aprons, which represent the most functionally and operationally critical elements of the airport infrastructure.

In **Step 5**, the HAZUS methodology (FEMA, 2022) was employed to estimate the probability of liquefaction under a selected seismic scenario. A magnitude Mw 6.3 earthquake associated with the nearby Kavala-Xanthi-Komotini fault system was chosen. Ground motion modelling was performed using REDAS software (Papatheodorou et al., 2023), based on input from the SHARE and GreDaas databases (Caputo et al., 2012; Giardini et al., 2013), producing a peak ground acceleration (PGA) value of 0.36g. Scenario fault rupture is considered as representative of strong onshore earthquakes in continental Greece, while these PGA values represent site surface conditions, using V_s30 grid (Greece V_s30 model developed by Stewart et al. (2014) using local geological and geotechnical data) and weighted GMPEs from Chiou and Youngs (2014) and Boore et al. (2021). They are also compatible with the 955-year return period results of the seismic hazard model of Thrace developed by Sotiriadis et al. (2023). Groundwater depth in the area of the airport was evaluated using a delta-wide borehole dataset derived from hydrogeological surveys conducted in 1978, complemented by more recent observations from the 2014 groundwater survey in the eastern part of the region (Ydroereuna, 1978; Stournaras, 1984; Ydrodomiki, 1985; Gkiougkis et al., 2021). The latter indicates that the piezometric surface of the phreatic/unconfined aquifer has risen in recent years, likely due to the abandonment of shallow boreholes and the adoption of surface irrigation and deeper boreholes (Gkiougkis et al., 2021). Considering these datasets, along with the known seasonal saturation patterns of the Holocene alluvial, fluvial, and coastal sediments that dominate the study area, groundwater depth was estimated to be generally less than 6 m. Given this input and the moment magnitude the conditional probability of liquefaction was calculated for each susceptibility class, classifying the site into four probability zones.

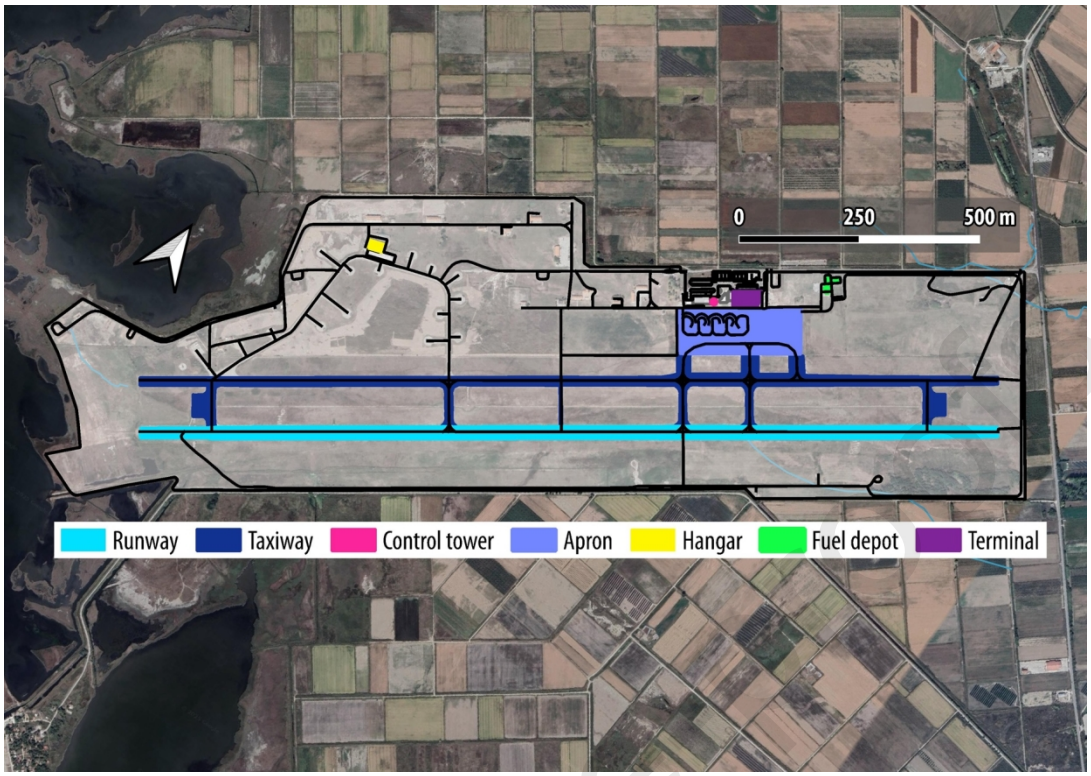

Figure 5: Critical components of KVA airport collected from Google Maps and Open Street Maps according to Step 4.

In **Step 6**, expected ground settlements PGD were estimated as the product of probability of liquefaction (PLsc) and the characteristic ground settlement amplitudes corresponding to each susceptibility class (Table 2). Emphasis was placed on zones of moderate to very high susceptibility, which overlap with critical airport infrastructure. Due to the inactivity of the surrounding channels and the lack of geomorphological features (i.e. point-bars), conducive to lateral spreading; the potential of liquefaction-induced horizontal deformation was considered negligible in the case of KVA.

Step 7 focused on assessing the vulnerability and expected losses associated with the estimated PGD values. The analysis concentrated on key airport components such as runways, taxiways, and apron areas. PGD was used as the hazard intensity measure to estimate the probability of exceeding slight-to-moderate, extensive, and complete damage levels, following the fragility functions and damage state thresholds defined in HAZUS (FEMA, 2022). Average damage ratios of 0.10, 0.40, and 0.80 were applied for each damage level respectively based on ranges of damage ratios proposed by HAZUS (Table 3). These were used to derive average loss ratios for each susceptibility class (Argyroudis, 2022), and, in turn, to compute the expected direct losses. Final loss estimations accounted for the affected area and the unit reconstruction costs of the relevant airport infrastructure.

Finally, in **Step 8**, the integrated outputs were used to produce a spatial risk profile for KVA, highlighting the most vulnerable zones of the airport under the selected earthquake scenario. This final step supports informed decision-making for inspection prioritisation, risk communication, and the development of targeted mitigation measures tailored to critical airport assets.

Table 3 Damage ratios for airport runways.

Damage State	Best Estimate Damage Ratio	Range of Damage Ratios
Slight	0.10	0.01 to 0.15
Moderate	0.40	0.14 to 0.40
Extensive	0.80	0.40 to 0.80
Complete	1.00	0.80 to 1.00

Results

Based on the spatial distribution of surficial geological units derived from the geomorphological mapping, the application of Youd and Perkins (1978) criteria resulted in the classification of the KVA area into four liquefaction susceptibility classes: low, moderate, high, and very high (Figure 4). Overlaying the airport infrastructure on this map revealed that approximately 300 m of the northwestern runway, 2.7 km of the adjacent taxiway, and 78 m² of the apron are located on an abandoned river branch—an area classified as very high susceptibility to liquefaction. The remaining facilities were predominantly situated on moderately susceptible floodplain deposits.

Using the HAZUS methodology (FEMA, 2022), the conditional probability of liquefaction for each susceptibility class under the selected seismic scenario (Mw 6.3, PGA = 0.36g, groundwater depth < 6 m) was estimated (Step 5). The calculated probabilities were: 0.20 for very high, 0.16 for high, 0.08 for moderate, and 0.03 for low susceptibility areas (Table 4, Figure 6). The corresponding expected permanent ground displacements (PGD) were computed by multiplying the probability of liquefaction by the characteristic settlement amplitude for each class. The results indicated average PGD values of 6.10 cm, 2.40 cm, 0.4 0 cm, and 0.10 cm for the very high, high, moderate, and low susceptibility classes, respectively (Table 4, Figure 6).

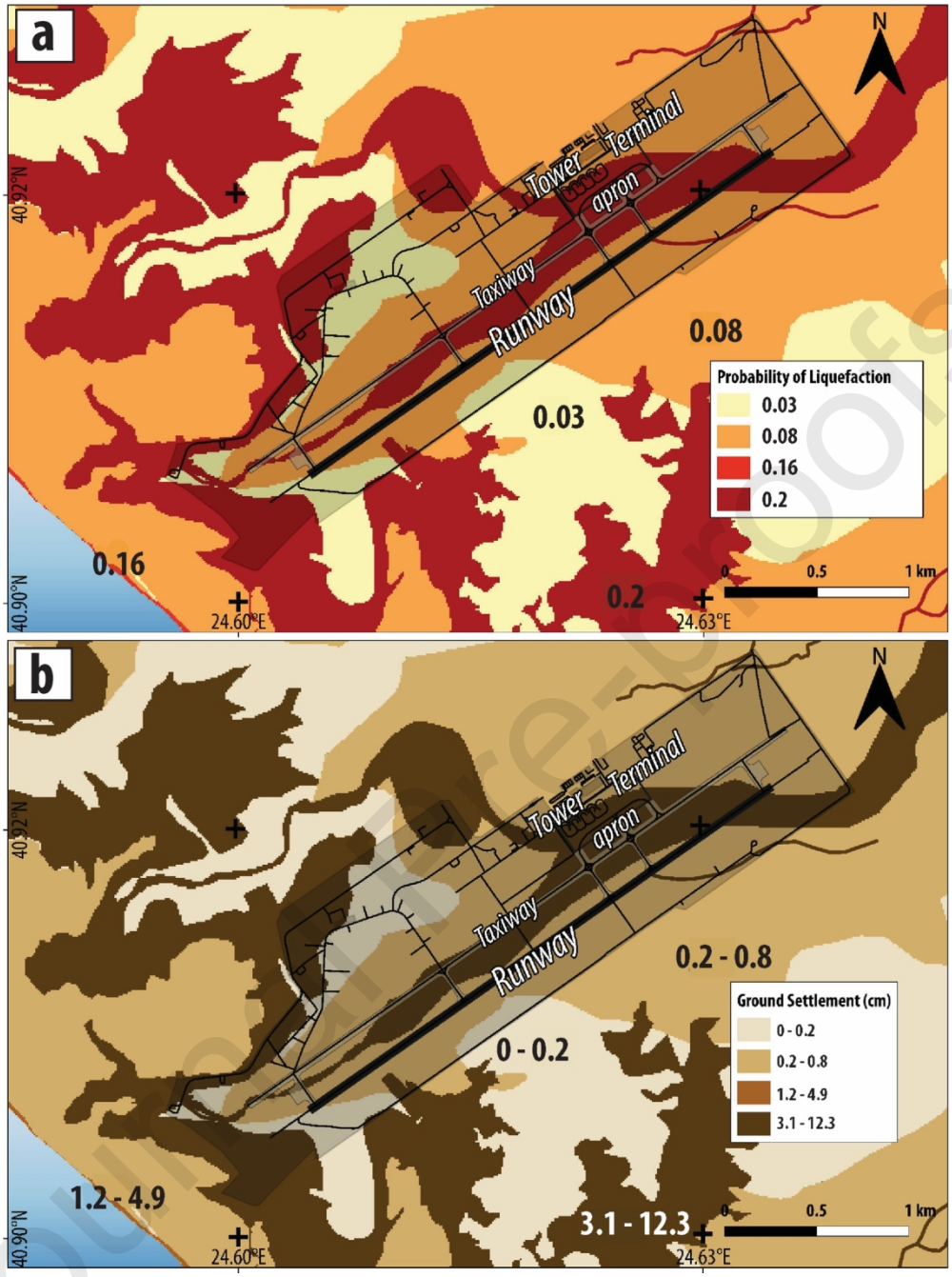

Figure 6: (a) Probability of liquefaction and (b) expected ground settlements in KVA area.

Given that critical airport infrastructure (runway, taxiway, apron) is located within moderate to very high susceptibility zones, these PGD estimates were used as intensity measures for evaluating damage probabilities in Step 7. The following PGD ranges were used: 0.2–0.8 cm for moderate zones and 3.1–12.3 cm for very high zones. These values were applied to estimate the probability of exceeding various damage states—slight/moderate, extensive, and complete—using HAZUS-defined fragility

functions. The average loss ratios associated with PGD values of 6.1 cm and 0.4 cm were calculated as 0.1534 and 0.0004, respectively.

In **Step 7**, these were used to compute direct losses by multiplying the loss ratios with the area of each infrastructure component and the corresponding reconstruction cost per m². The following reconstruction costs were considered: €186/m² for asphalt-paved runway (3,000 × 45 m²), €164/m² for taxiway (4,000 × 35 m²), and €164/m² for apron (96,000 m²). Reconstruction costs (Table 5) were derived from the airport pavement cost tables of Markovich (2011). The 2011 U.S. values were updated to 2024 using inflation indices and adjusted to the Greek context using PPP factors. As shown in Table 5, the estimated direct losses were €0.37 million for the runway, €2.5 million for the taxiway, and €2.0 million for the apron, leading to a total expected loss of approximately €5 million for the defined seismic scenario. Loss ranges reflect the variation in PGD and associated damage states across the different susceptibility zones.

Table 4 Estimated liquefaction probabilities and ground settlements (PGD) based on HAZUS methodology. The moment magnitude (K_M) and groundwater (K_W) correction factors are: K_M=1.2, K_W=1.0.

Susceptibility Class	$P[Liquefaction_{sc}\|PGA=a]$	P_{ml}	PLsc	PGD amplitude (cm)	Expected PGD (cm)	Range (cm)
Very High (VH)	$0 \le 9.09a - 0.82 \le 1.0$	0.25	0.20	30.50	6.10	3.10–12.30
High (H)	$0 \le 7.67a - 0.92 \le 1.0$	0.20	0.16	15.20	2.40	1.20–4.90
Moderate (M)	$0 \le 6.67a - 1.0 \le 1.0$	0.10	0.08	5.10	0.40	0.20–0.80
Low (L)	$0 \le 5.57a - 1.18 \le 1.0$	0.05	0.03	2.50	0.10	0.00–0.20

Table 5 Estimated direct losses for KVA airport infrastructure.

Facility	PGD (cm)	Area (m²)	Avg. loss ratio	Reconstruction cost (€/m²)	Direct loss (€)	Loss range (€)

Runway	0.2–0.8	122,247	0.0004	186	8,300	0 – 50,900
	3.1–12.3	12,753	0.1534	186	363,400	162,700–737,100
Taxiway	0.2–0.8	45,513	0.0004	164	2,728	0–16,700
	3.1–12.3	99,489	0.1543	164	2,534,000	1,100,000–5,100,000
Apron	0.2–0.8	17,605	0.0004	164	1,100	0–6,500
	3.1–12.3	78,468	0.1534	164	1,900,000	883,900–4,000,000
Total					€5.0 million	€2.2 – €9.9 million

The spatial risk profile for KVA enables targeted inspection planning and resilience measures (Step 8), focusing on infrastructure segments located in areas of high liquefaction susceptibility and ground deformation. This facilitates prioritisation of mitigation measures, including soil stabilisation or drainage improvements, particularly in zones underlain by abandoned river channels and deltaic deposits. The framework also supports scenario-based assessments, allowing comparisons across different earthquake magnitudes or fault sources, as well as other threats for enhancing long-term resilience planning (Trump et al., 2025) by airport operators, insurers and investors.

Validation

Historical earthquake events—including the 1989 Loma Prieta (USA), 2001 Nisqually (USA), and 2023 Turkey–Syria earthquakes—have highlighted the vulnerability of airports to secondary seismic hazards such as soil liquefaction. In particular, Oakland International Airport (OAK), King County International Airport (BFI), and Hatay International Airport (HTY) experienced extensive damage, including pavement cracking, subsidence, and ground surface discontinuities. To validate the methodology applied at Kavala International Airport (KVA), a comparative analysis was conducted using available data from these past events. The HAZUS framework was used to simulate liquefaction

susceptibility and associated risk at each airport, allowing for a benchmark comparison with the KVA results and demonstrating the applicability and reliability of the proposed approach.

It should be acknowledged that HAZUS was originally developed for U.S. conditions, which introduces uncertainties when applying its soil parameters, liquefaction probability factors (KM, KW, Pml), or settlement amplitudes to other regions. However, these formulations are based on empirical relationships widely used internationally, and their transferability is supported here through validation at three well-documented liquefaction-affected airports (OAK, BFI, HTY). In all cases, the predicted susceptibility, liquefaction probability, and PGD ranges showed strong consistency with observed field displacements, indicating that HAZUS can provide reliable regional-scale screening in diverse sedimentary settings. Nonetheless, we recognise that site-specific applications would benefit from future calibration using local CPT/SPT and groundwater data.

Oakland International Airport (OAK)

Oakland International Airport (OAK) is situated along the eastern shore of San Francisco Bay in western Alameda County. Geological and historical maps indicate that the airport is built across former tidal marshes, tidal flats, and shallow bay environments (SFEI, 2000). Subsurface materials primarily consist of Holocene estuarine deposits, Holocene and Pleistocene alluvial deposits, and the late Pleistocene to early Holocene Merritt Sand (Lajoie and Helley, 1975; Helley and Lajoie, 1979; Witter et al., 2006). The northeastern portion of the airport, which represents the original facility footprint, lies over marshland influenced by deltaic and stream channel deposits from San Leandro Creek. Conversely, the southwestern section is constructed on fill placed over former tidal flats and shallow bay muds. The artificial fill consists of loose to dense sand, silty sand, and stiff to medium stiff silt and clay, with variable gravel content. Its thickness ranges from 2.5–4 m in the southern sector to 0.3–2 m in the north (AGS, 2008).

On October 17, 1989, the Mw 6.9 Loma Prieta earthquake struck approximately 80 km from the OAK site, triggering widespread liquefaction across the Bay Area and causing significant damage to airport infrastructure. One of the most affected facilities was the 3-km main runway (11–29), built on hydraulic fill over Bay mud. Approximately 900 m of its northwestern section exhibited sand boils, pavement buckling, and vertical and lateral displacements of 20 cm and 60 cm, respectively (Vallegra et al., 1992). The western end of the runway was also laterally shifted by about 60 cm, while the adjacent taxiway sustained 30 cm pavement cracks and 15 cm of vertical settlement (Holzer, 1998). Ground cracks and liquefaction ejecta zones, with typical lengths of up to 70 m, were documented (Figures 7, Figure 8).

The primary factors contributing to these failures included the shallow water table, uniform gradation of fill material, and the presence of saturated, relatively loose sand layers beneath the fill. Additional liquefaction effects were reported at the main terminal building, where sand intrusion was observed in an annex, and at a nearby taxiway, which experienced settlements of up to 8 cm (Holzer, 1998; Seed et al., 1991). The total repair costs were approximately $3.5 million for the runway and $2.2 million for the taxiway (Plafker and Galloway, 1998).

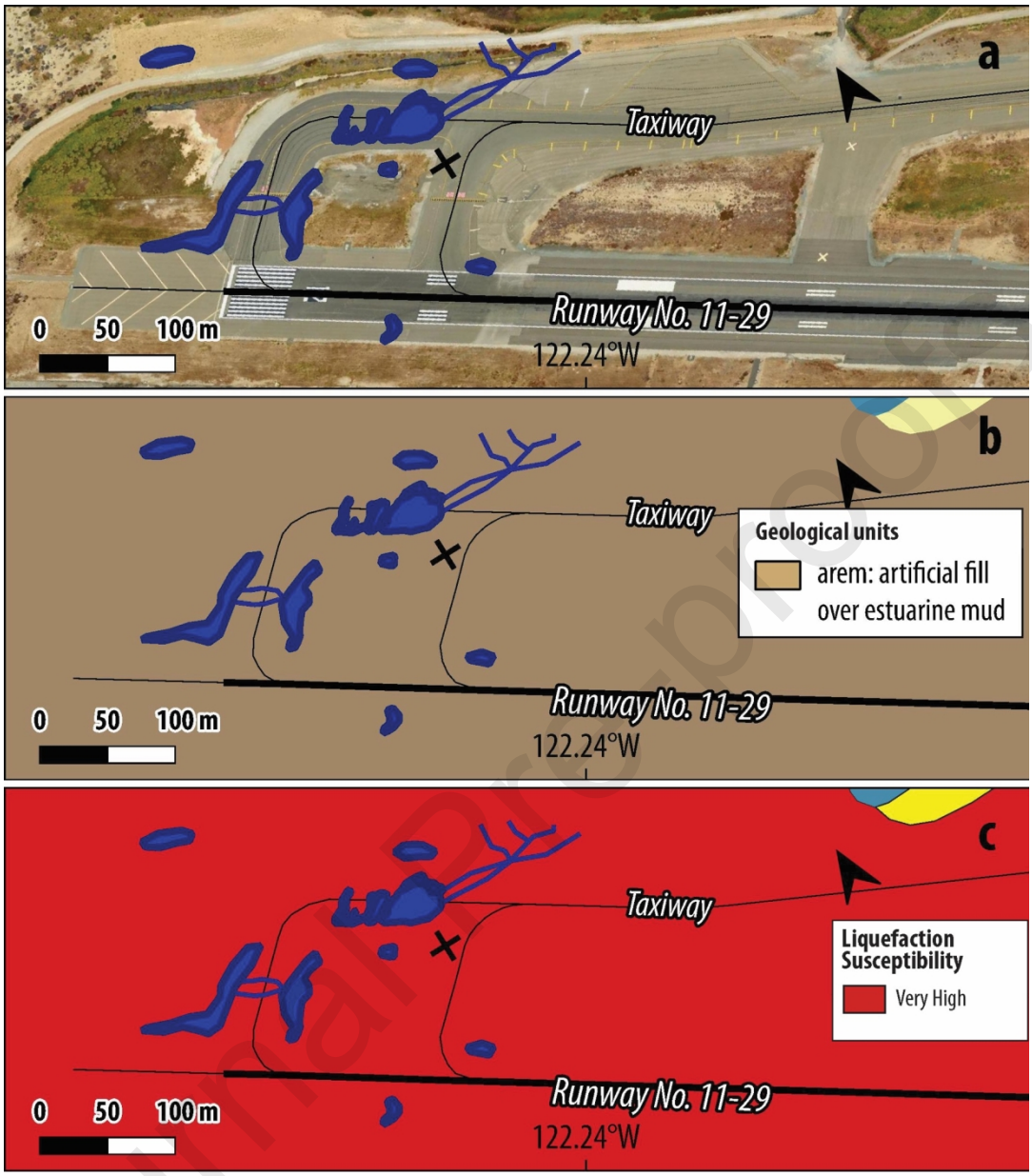

Figure 7: Liquefaction ejecta and ground cracking (blue zones) at OAK following the 1989 Loma Prieta earthquake, projected onto: (a) satellite imagery, (b) geological units map, and (c) liquefaction susceptibility map (modified after William Lettis and Associates, 1999).

Application of the HAZUS methodology to the OAK site showed strong consistency with these observed impacts. The resulting liquefaction susceptibility map classified most of the airport as highly susceptible, and the HAZUS-based analysis estimated a probability of liquefaction of 0.22, with expected ground settlements ranging from 3.40 to 13.60 cm (Table 6; Figure 8). These outcomes closely align with the recorded displacements and field damage reports, supporting the validity of the applied methodology.

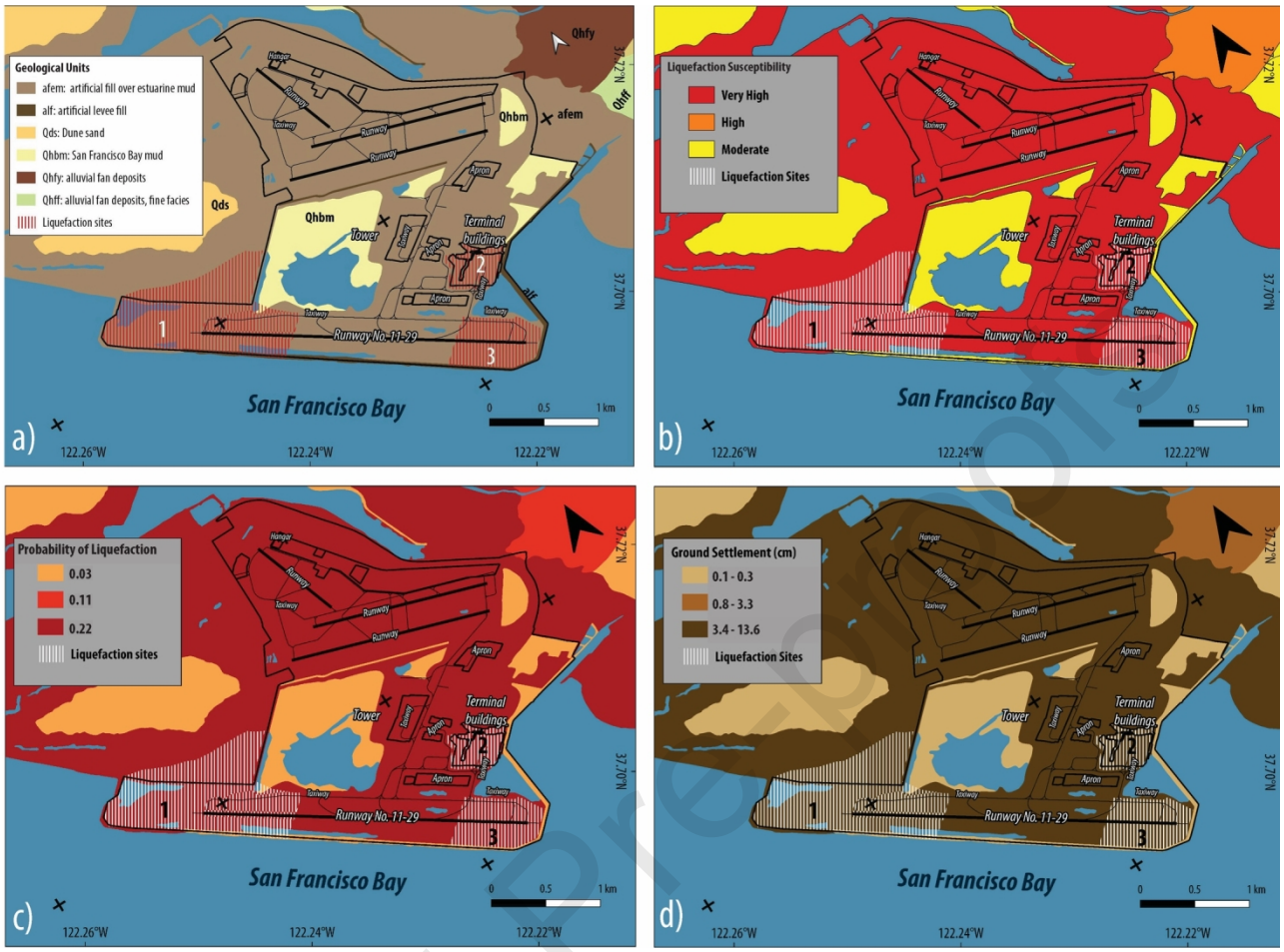

Figure 8: Liquefaction manifestations at OAK based on: (a) geological units, (b) liquefaction susceptibility, (c) liquefaction probability, and (d) ground settlement (modified after Witter et al., 2006).

King County International Airport (BFI)

King County International Airport (BFI), also known as Boeing Field, is located within the Duwamish River corridor, south of downtown Seattle, Washington. The area has undergone extensive anthropogenic modification, particularly between 1890 and 1930, during which time natural features such as meanders, tidal flats, depressions, and the river mouth were filled through hydraulic placement (Beetham et al., 2001). The airport is situated on Quaternary alluvial sediments, with parts of its infrastructure—most notably sections of the runway—constructed over abandoned meander channels, which are known to have elevated liquefaction potential. Following the Mw 6.8 Nisqually earthquake in 2001, BFI experienced widespread liquefaction (Nisqually Earthquake Clearinghouse Group, 2001; Bray et al., 2001).

Application of the HAZUS methodology indicated that BFI predominantly falls within the high susceptibility class, with a liquefaction probability of 0.08, while the portion of the runway situated on the abandoned meander was classified as very high susceptibility, with an estimated probability of 0.17. The corresponding ground settlement estimates ranged from 0.60 to 2.30 cm in high susceptibility zones, and from 2.50 to 10.20 cm in the

very high zones. The spatial projection of affected areas onto susceptibility, probability, and settlement maps confirmed a high degree of consistency between HAZUS-based predictions and observed field damage (Table 6, Figure 9).

Liquefaction effects were most pronounced along the eastern runway, where sand ejecta fields extended approximately 90 m, and ground surface settlements reached up to 20 cm. In contrast, the western runway was impacted by only a few isolated sand boils. Notably, the northern portion of the airfield experienced the formation of a sinkhole approximately 1.2 m wide and 1.8 m deep. These features were attributed to cyclic ground oscillations, which also resulted in pavement cracking at the joints along both runways. A particularly significant longitudinal crack, measuring nearly 305 m in length and 1.2 to 2.5 cm in width, was observed along the western edge of the western runway. The spatial distribution of these manifestations closely followed the course of a former Duwamish River meander, reinforcing the importance of geomorphological history in assessing liquefaction vulnerability.

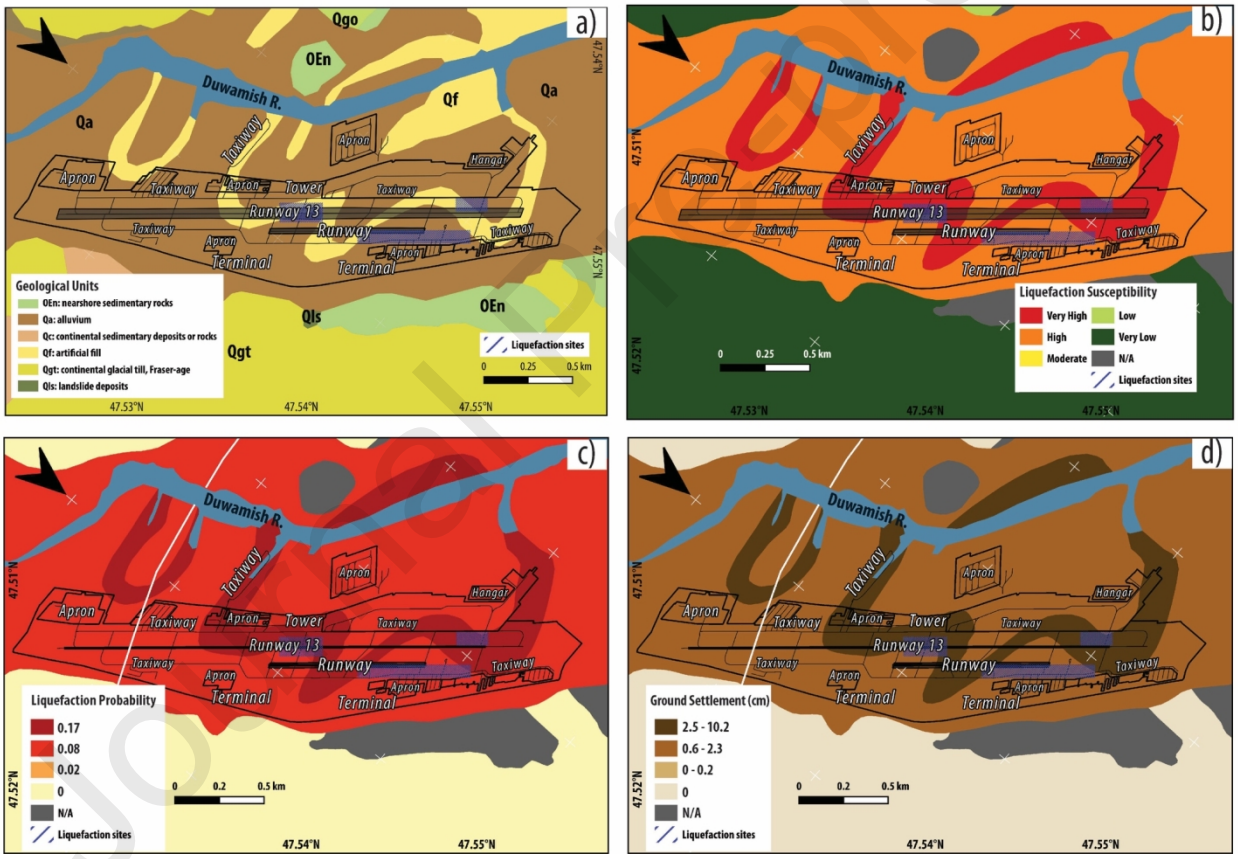

Figure 9: Liquefaction manifestations of the 2001 Nisqually earthquake at BFI Airport, based on maps of: (a) geological units, (b) liquefaction susceptibility, (c) liquefaction probability, and (d) ground settlement (modified after Washington Division of Geology and Earth Resources, 2016).

Hatay International Airport (HTY)

HTY is located in the western Amik Plain, on the former lakebed of Amik Lake (Kilic et al., 2006). The geological setting reflects significant lacustrine and fluvial influences, with the lake's floor now consisting predominantly of fine-grained sediments—including silts of low to medium plasticity with varying clay content—extending to depths of up to 30 m (Bol et al., 2024). Following the 2023 Türkiye–Syria earthquake doublet—which involved two major earthquakes (Mw 7.7 and Mw 7.6) along the East Anatolian Fault Zone (EAFZ)—HTY experienced both surface rupture and liquefaction-induced ground displacements (Figure 7). In the western section of the airport, a series of ground cracks oriented southwest were observed, attributed to a surface rupture along a previously unmapped segment of the Dead Sea Fault Zone (DAFZ) (Taftsoglou et al., 2023). The surface ruptures may have facilitated the upward movement of liquefied material, contributing to the formation of sand ejecta. Given the combination of strong ground shaking and the mechanical properties of the underlying fine-grained sediments, the HTY site was particularly prone to deformation. Furthermore, as observed in the 1999 Kocaeli earthquake (Bol, 2003), the development of surface ruptures may have been influenced by differential settlement, likely resulting from variations in sediment thickness between the eastern and western parts of the airport.

In contrast, the eastern part of the airport exhibited classic liquefaction and shaking-induced deformation. Field surveys documented vertical displacements of 30–40 cm and horizontal shifts of 10–15 cm (Bol et al., 2024). These ground movements, along with visible cracks and craters on the runway and adjacent infrastructure, resulted in the closure of the airport for six days. Detailed inspection revealed 12 transverse ground cracks with associated sand ejecta on the runway, and an additional seven liquefaction sites on the central taxiways and apron (Figure 11). The average length of runway cracks was 45 m, with a regular spacing pattern of approximately 100 m in the middle section and 150 m in the eastern part.

The spatial projection of these field observations onto the HAZUS based - generated maps confirmed the accuracy of the methodology. Nearly the entire airport infrastructure was classified as very highly susceptible to liquefaction, with an estimated liquefaction probability of 0.24 and expected ground settlements ranging from 3.60 to 14.40 cm (Table 6, Figure 10). The alignment between observed damage and modelled outputs provides additional confidence in the methodology's applicability to data-sparse, geologically sensitive regions like HTY.

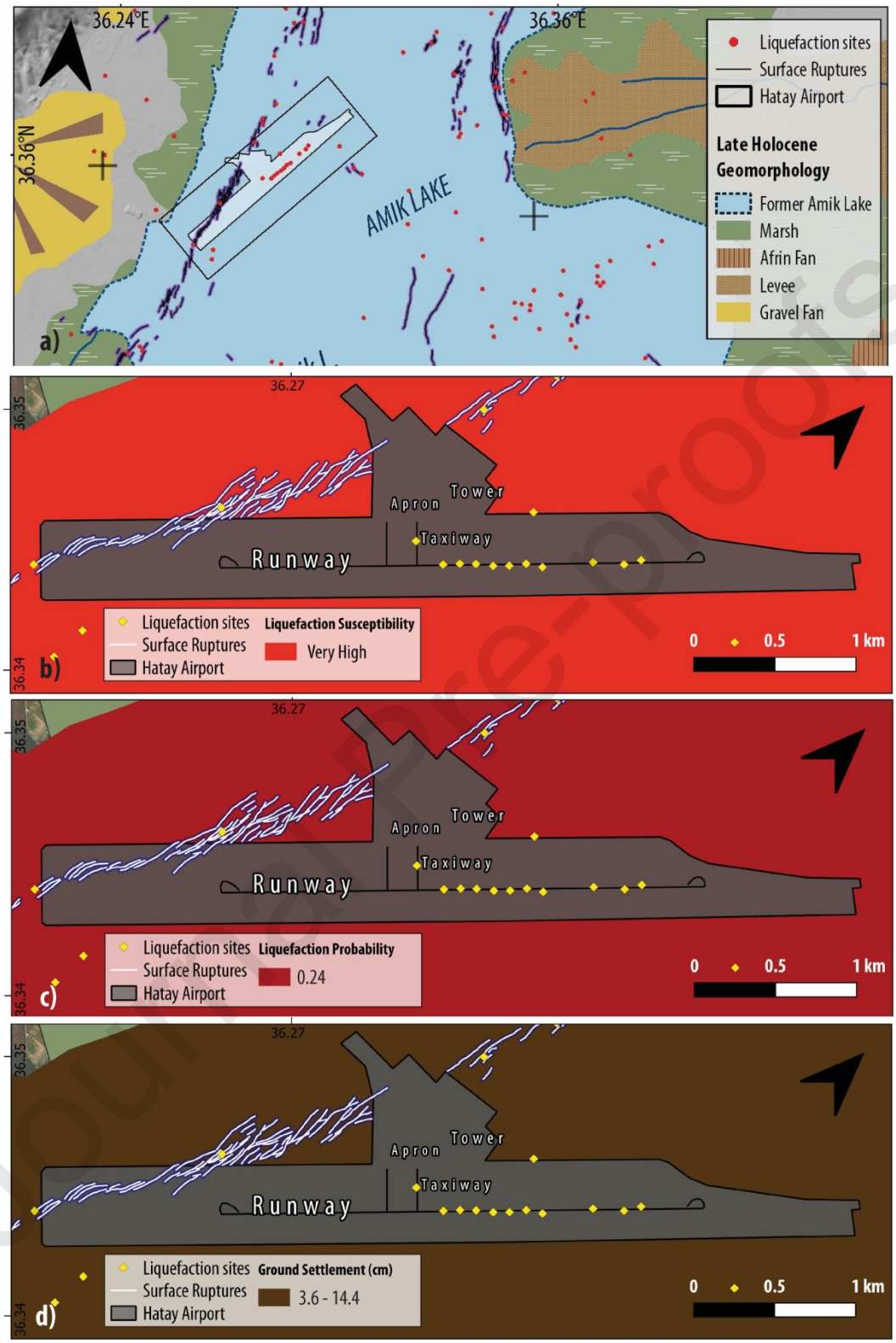
36.24°E
36.36°E
36.36°N
AMIK LAKE
Liquefaction sites
Surface Ruptures
Hatay Airport
Late Holocene Geomorphology
Former Amik Lake
Marsh
Afrin Fan
Levee
Gravel Fan
a)
36.27
36.35
36.34
Apron
Tower
Taxiway
Runway
Liquefaction sites
Surface Ruptures
Hatay Airport
Liquefaction Susceptibility
Very High
0
0.5
1 km
b)
Liquefaction Probability
0.24
c)
Ground Settlement (cm)
3.6 - 14.4
d)

Figure 10: Liquefaction manifestations of the 2023 Türkiye–Syria earthquake doublet at HTY Airport, based on maps of: (a) geological units (modified after Taftsoglou et al., 2023), (b) liquefaction susceptibility, (c) liquefaction probability, and (d) ground settlement.

Figure 11: Satellite view of the HTY airport area. Yellow and red index zones indicate: (a) surface ruptures located on the western side of the runway, and (b) transverse ground cracks and sand ejecta observed along the central and eastern sections of the runway and parts of the taxiway (modified after Bol et al., 2024).

Table 6 Estimation of liquefaction probability (PLsc) and expected permanent ground displacement (PGD) for KVA, OAK, BFI, and HTY airports, based on the FEMA (2022) methodology and categorised by susceptibility class (SC). Asterisks (*) indicate susceptibility classes that intersect directly with critical airport infrastructure (e.g. runways, taxiways, aprons).

Earthquake	KVA (scenario)	OAK (17/09/1989)	BFI (28/02/2001)	HTY (06/02/2023)	
PGA (g)	0.36	0.20	0.18	0.80	
Mw	6.30	6.90	6.80	7.70	
K_W	1.00	1.00	1.10	1.10	
K_M	1.20	1.10	1.10	1.00	
SC Class	PLsc				P_{ml}
Very High (VH)	0.20*	0.22*	0.17*	0.24*	0.25
High (H)	0.16	0.11*	0.08*	0.19	0.20
Moderate (M)	0.08*	0.03*	0.02	0.10	0.10
Low (L)	0.03*	0.00	0.00	0.05	0.05
SC Class	Expected PGA (cm)				PGD (settlement) amplitude (cm)

Very High (VH)	3.10–12.30*	3.40–13.60*	2.50–10.20*	3.60–14.40*	30.50
High (H)	1.20–4.90	0.80–3.30*	0.60–2.30*	1.40–5.70	15.20
Moderate (M)	0.20-0.80*	0.10–0.30*	0.00–0.20	0.20–1.00	5.10
Low (L)	0.00–0.20*	0.00	0.00	0.10–0.20	2.50

Discussion

The cases of OAK, BFI, and HTY airports represent well-documented examples of liquefaction-induced damage to critical transportation infrastructure. These datasets were instrumental in validating the methodology proposed in this study. A comparison of observed and predicted outcomes revealed that liquefaction manifestations consistently occurred within areas classified as “very high susceptibility” by the HAZUS-based framework. This supports the reliability of the susceptibility mapping and risk estimation approach. However, the extent of observed damage was generally more localised than the predicted susceptible zones. This discrepancy highlights the influence of data availability and spatial resolution on validation outcomes. For OAK and BFI, damage was documented as generalised zones of liquefaction, while in HTY, liquefaction manifestations were reported as specific discrete sites. This difference in documentation scale introduced a level of qualitative comparison, rather than precise spatial matching between observed and predicted extents.

Across both the KVA case study and the three validation airports (OAK, BFI, HTY), the spatial patterns of predicted PGD consistently align with operationally sensitive pavement nodes such as runway–taxiway intersections, turning segments, and apron transition zones. These areas coincide with underlying geomorphological weaknesses—abandoned channels, reclaimed tidal flats, and fine-grained lacustrine deposits—where liquefaction-induced settlement tends to localise. Even moderate PGD levels can affect braking efficiency, pavement evenness, and safe aircraft manoeuvring, while higher PGD concentrations may necessitate temporary closure or traffic restrictions. The consistency of these patterns across four international airports highlights the practical value of PGD mapping not only for damage estimation but also for identifying critical points where liquefaction-related deformation is most likely to impair airport operability.

Given the airport runway is both functionally critical and, as shown in all three cases, highly vulnerable to liquefaction, this component was selected as a focal point for spatial

comparison. The correlation between predicted and observed runway failures is presented in Table 7 and summarised in Figure 12.

- At OAK, the runway lies entirely within the very high susceptibility zone. Observed damage affected approximately 53.4% of the total predicted susceptible area, indicating a relatively strong match between modelled and observed impact.
- At BFI, the runway spans both very high and high susceptibility zones. The total predicted liquefiable area was estimated at 3.8×10^5 m², yet only 0.37×10^5 m² was reported as affected—representing 18.2% and 5.8% of the very high and high zones, respectively. This partial correlation reflects the spatial heterogeneity of the liquefaction process and possibly unreported minor manifestations. Liquefaction is often patchy**,** controlled by local soil layering, groundwater variations, and non-uniform cyclic stress levels—factors that static surrogate models like HAZUS may not capture (Maurer et al., 2015).
- At HTY, the entire runway falls within the very high susceptibility class. While the model predicted failure over an area of 1.85×10^5 m², only 0.06×10^5 m² (approximately 3.2%) was documented as affected. This can be attributed to the coarse granularity of the data—damage reports were limited to discrete “sites” rather than continuous zones, unlike the zone-based observations at OAK and BFI—and to the high spatial variability in sediment characteristics and groundwater depth. Similar discrepancies between predicted and observed extents have been noted in regional liquefaction studies, where fine-scale heterogeneity leads to over-prediction by geospatial models.

To incorporate quantitative spatial validation, we computed the overlap area between the predicted liquefaction-susceptible runway zones (VH or VH+H) and the mapped footprints of observed liquefaction damage at OAK, BFI, and HTY. In all three cases, the observed failures were entirely contained within the predicted susceptible areas, meaning that the overlap area equals the observed area. Based on this intersection, three performance indicators were derived: (i) True Positive Rate (TPR), defined as the overlap area divided by the total observed damaged area (TPR = overlap/observed); (ii) Precision, defined as the proportion of the predicted susceptible area that corresponds to observed failures (Precision = overlap/predicted); and (iii) Intersection-over-Union (IoU), which measures spatial agreement between predicted and observed extents (IoU = overlap/(predicted + observed − overlap)). These indicators, reported in Table 7, show high spatial consistency at OAK and BFI (higher Precision and IoU values) and lower agreement for HTY, reflecting the smaller and more localised nature of observed manifestations there.

These findings underline the importance of data resolution, geomorphological variability**,** and ground investigation density in validating susceptibility models. Despite these limitations, the results demonstrate that the proposed methodology provides a robust framework for identifying high-risk areas and supporting prioritised mitigation planning. Yet, the observed discrepancies described above highlight the necessity of interpreting susceptibility and risk maps as first-pass screening tools. For infrastructure planning, overlaying predicted zones with targeted site investigations (e.g., CPT, shear-wave velocity) is essential to refine risk assessments (Juang et al., 2013). Moreover,

adopting probabilistic models that incorporate geotechnical variability can yield more accurate, site-specific predictions.

Table 7 Quantitative validation of predicted (PR) versus observed (OB) liquefaction-induced runway failures for OAK, BFI, and HTY airports. The table reports the overlap area and derived performance indicators—True Positive Rate (TPR), Precision, and Intersection-over-Union (IoU)—to assess spatial agreement between predicted susceptible zones and mapped damage extents. Asterisks (*) indicate combined totals for the very high (VH) and high (H) susceptibility classes at BFI.

Airport	SC	PR failures ($x10^5 m^2$)	OB failures ($x10^5 m^2$)	OB failures (%)	Precision (%)	IoU	TRP
OAK	VH	2.81	1.50	53.40	53.40	0.53	1.00
BFI	VH	1.21	0.22	18.20	18.20	0.82	1.00
	H	2.59	0.15	5.80	5.80	0.06	1.00
	VH+H	3.80*	0.37*	24.00*	24.00*	0.10*	1.00
HTY	VH	1.85	0.06	3.20	3.20	0.03	1.00

Conclusions

This study presents a scalable and rapid framework for assessing airport infrastructure risk due to seismic-induced soil liquefaction, by integrating multi-modal data sources—including geological maps, remote sensing imagery, digital elevation models, and open-access infrastructure data. The proposed nine-step methodology offers a data-efficient and reproducible approach to identifying and quantifying liquefaction susceptibility, ground deformation, and potential losses in critical airport assets. The methodology was applied to Kavala International Airport (KVA) in northern Greece. Using remote sensing and geological datasets, a geomorphological base map was developed and used to classify surficial units by age and depositional environment. Liquefaction susceptibility was mapped using Youd and Perkins (1978) criteria, identifying very high and moderate susceptibility zones that coincide with major airport components such as the runway, taxiway, and apron. Based on a representative seismic scenario (Mw 6.3), the probability of liquefaction was estimated as 0.2 for the most critical zones, with expected ground settlements (PGD) reaching 6.1 cm. Total direct losses were estimated at €5 million, with the taxiway and apron accounting for the largest share.

Validation using historical earthquake cases at Oakland (OAK), King County (BFI), and Hatay (HTY) International Airports confirmed the method's reliability: observed damage aligned with areas predicted to be highly susceptible to liquefaction. However, the spatial extent of observed damage was more localised than predicted, due to factors such as subsurface heterogeneity, groundwater variability, shaking intensity, and differences in data resolution. Notably, at HTY, the limited spatial footprint of documented failures reflected the granularity of point-based field reports, as opposed to the zone-based data available at OAK and BFI.

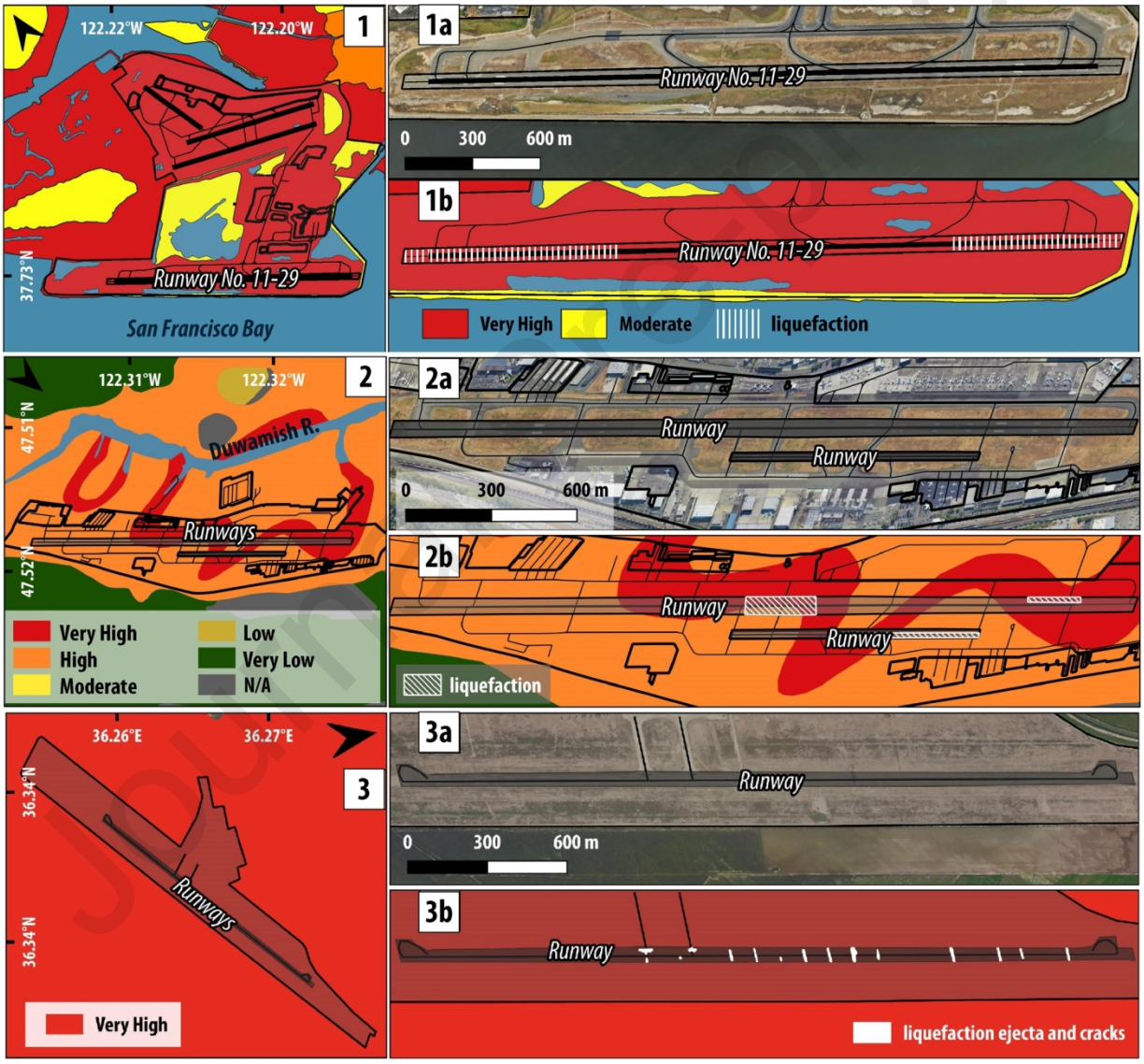

Figure 12: Liquefaction susceptibility classes overlaid with observed liquefaction records along the runways of: (1) Oakland International Airport (OAK), (2) King County International Airport

(BFI), and (3) Hatay International Airport (HTY). The figure highlights the spatial correspondence between predicted susceptibility zones and recorded liquefaction damage.

This framework offers a risk screening tool that can be applied at national, regional, or global scales to assess critical airport infrastructure located in liquefaction-prone areas, particularly within coastal zones. By integrating multi-modal datasets—including geomorphological, remote sensing, and open-access infrastructure data—it provides a practical, scalable solution for both data-rich and data-limited contexts. The methodology aligns with cascading hazard perspectives (Yanites et al., 2025), where liquefaction may interact with or be compounded by hazards such as flooding, sea-level rise, and infrastructure interdependencies. Moreover, the framework is adaptable to climate-sensitive contexts, where sea-level rise and increased groundwater levels can elevate the probability and severity of liquefaction. In this way, it contributes to a broader understanding of the airport as a resilient ecosystem (Horton et al., 2025), by linking physical risk assessment with operational preparedness and strategic planning. The approach enables stakeholders to identify critical vulnerabilities, prioritise mitigation, and support long-term resilience, ultimately strengthening the capacity of airports to function under multiple, interacting stressors in an evolving Earth and climate system.

This study has some limitations that should be acknowledged. One constraint is that the HAZUS framework was originally calibrated for U.S. geological conditions and infrastructure typologies, which may differ from those present in other regions; although its empirical formulations for liquefaction triggering, settlement, and vulnerability are widely used internationally, regional variations in soil properties, groundwater regimes, and pavement design practices may influence accuracy. The multi-site validation across three airports helps mitigate this limitation, demonstrating consistency between predicted susceptibility patterns, PGD ranges, and observed liquefaction manifestations.

An additional source of uncertainty arises from the liquefaction susceptibility map itself, which depends on the level of detail available in the geomorphological mapping of the study area. Because the delineation of geomorphological units influences the classification of susceptibility zones, minor variations may occur depending on the scale and resolution of the remote sensing and geological datasets originally used. These variations may affect the estimated liquefaction probability for the airport and, consequently, the predicted permanent ground deformations (PGD). To account for this uncertainty, the analysis includes proposed ranges of maximum and minimum expected settlement rather than relying on a single deterministic value.

Furthermore, limitations relate to the input groundwater and geomorphological datasets, which may not fully capture seasonal variability, long-term trends, or climate-driven changes, while post-event damage reporting varies in detail and spatial completeness. Future research should therefore prioritise improved hydrogeological and geomorphological datasets, integration of probabilistic seismic scenarios, and assessment of interactions with other hazards—such as flooding, sea-level rise, or subsidence—to enhance the framework's adaptability to multi-hazard and climate-sensitive contexts. Finally, expanding and testing the methodology across other critical

infrastructure types, such as ports, highways, or railways, and in diverse tectonic and environmental settings would further strengthen its applicability as a regional- and global-scale screening tool.

Acknowledgements

The first three authors acknowledge support of this work by the project “Risk and Resilience Assessment Center–Prefecture of East Macedonia and Thrace-Greece.” (MIS 5047293) which is implemented under the Action “Reinforcement of the Research and Innovation Infrastructure”, funded by the Operational Programme “Competitiveness, Entrepreneurship and Innovation” (NSRF 2014-2020) and co-financed by Greece and the European Union (European Regional Development Fund).

Declaration of competing interest

The authors declare that they have no known competing financial interests or personal relationships that could have appeared to influence the work reported in this paper.

Data availability

Data will be made available on request

References

Adler M, Petrat A, Jongeling A, Kiefer M, De Jong G, Behrens C, et al. The economic and social impact of European airports and air connectivity. ACI EUROPE, SEO Amsterdam Economics; 2024. Report No. 978-90-5220-453-6.

AGS. Technical Memorandum No. 2: Geotechnical Study for Runway Safety Areas, Oakland International Airport; 2008.

Albano M, Chiaradonna A, Saroli M, Moro M, Pepe A, Solaro G. InSAR analysis of post-liquefaction consolidation subsidence after 2012 Emilia earthquake sequence (Italy). Remote Sens 2024;16:2364. https://doi.org/10.3390/rs16132364

Amanta AS, Dasaka SM. Air injection method as a liquefaction countermeasure for saturated granular soils. Transp Geotech 2021;30:100622. https://doi.org/10.1016/j.trgeo.2021.100622

Argyroudis SA. Resilience metrics for transport networks: A review and practical examples for bridges. Proc Inst Civ Eng - Bridge Eng 2022;175(3):179–192. https://doi.org/10.1680/jbren.21.00075

Barnhart WD, Yeck WL, McNamara DE. Induced earthquake and liquefaction hazards in Oklahoma, USA: Constraints from InSAR. Remote Sens Environ 2018;218:1–12. https://doi.org/10.1016/j.rse.2018.09.005

Bastin S, Stringer ME, Green RA, Wotherspoon L, van Ballegooy S, Cox BR, et al. Geomorphological controls on the distribution of liquefaction in Blenheim, New Zealand, during the 2016 Mw7.8 Kaikoura Earthquake. In: Geotechnical Earthquake Engineering and Soil Dynamics V. Reston, VA: American Society of Civil Engineers; 2018. p. 264–72. https://doi.org/10.1061/9780784481455.026

Bastin SH, Quigley MC, Bassett K. Paleoliquefaction in Christchurch, New Zealand. Bull Geol Soc Am 2015;127(9–10):1348–60.

Beaty M, Byrne P. An effective stress model for predicting liquefaction behaviour of sand. Geotech Earthq Eng Soil Dyn III 1998;75(1):766–777.

Beetham D, Beattie G, Earl B, Duncan D. NZ society for earthquake engineering reconnaissance team to Seattle, USA: The February 28, 2001 Nisqually earthquake. Bull N Z Soc Earthq Eng 2001;34(4):253–75. https://doi.org/10.5459/bnzsee.34.4.253-275

Bol E, Özocak A, Sert S, Çetin KÖ, Arslan E, Kocaman K, et al.. Evaluation of soil liquefaction in the city of Hatay triggered after the February 6, 2023 Kahramanmaraş–Türkiye earthquake sequence. Eng Geol 2024;339:107648. https://doi.org/10.1016/j.enggeo.2024.107648

Bol E. The geotechnical properties of Adapazari soils (in Turkish). Graduate thesis. Adapazari: Sakarya University; 2003.

Boore D, Stewart J, Skarlatoudis A, Seyhan E, Margaris B, Theodoulidis N, et al. A ground-motion prediction model for shallow crustal earthquakes in Greece. Bull Seismol Soc Am 2021;111(2):857–874. https://doi.org/10.1785/0120200270

Boulanger RW, Idriss IM. CPT and SPT based liquefaction triggering procedures. Report No. UCD/CGM-14/01. Center for Geotechnical Modeling, University of California, Davis; 2014.

Boulanger RW, Ziotopoulou K. PM4Sand (Version 3.1): A sand plasticity model for earthquake engineering applications. Report No. UCD/CGM-17/01. Center for Geotechnical Modeling, Department of Civil and Environmental Engineering, University of California, Davis; 2017.

Brady RJ, Perkins JB. Macroeconomic effects of the Loma Prieta Earthquake. In: The Loma Prieta, California, Earthquake of October 17, 1989 – Recovery, Mitigation, and Reconstruction. U.S. Geological Survey Professional Paper 1553-D; 1998. p. D3–16.

Bray JD, Sancio RB, Kammerer AM, Merry S, Rodriguez-Marek A, Khazai B, et al. Some observations of geotechnical aspects of the February 28, 2001 Nisqually Earthquake in Olympia, South Seattle, and Tacoma, Washington; 2001. http://peer.berkeley.edu/nisqually/geotech

Byrne PM. A cyclic shear-volume coupling and pore-pressure model for sand. In: Proceedings of the Second International Conference on Recent Advances in Geotechnical Earthquake Engineering and Soil Dynamics, St. Louis, MO, USA, 11–15 March 1991; 1991. p. 47–55.

Caputo R, Chatzipetros A, Pavlides S, Sboras S. The Greek Database of Seismogenic Sources (GreDaSS): State-of-the-art for northern Greece. Ann Geophys 2012;55(5):859–894. https://doi.org/10.4401/ag-5168.

Caputo R, Helly B, Rapti D, Valkaniotis S. Late Quaternary hydrographic evolution in Thessaly (Central Greece): The crucial role of the Piniada Valley. Quat Int 2021;635:3–19. https://doi.org/10.1016/j.quaint.2021.02.013.

CDMG. Guidelines for analyzing and mitigating liquefaction hazards in California. California Department of Conservation, Division of Mines and Geology, Special Publication 117; 1999.

Cetin KO, Seed RB, Der Kiureghian A, Tokimatsu K, Harder LF, Kayen RE, et al. Standard penetration test-based probabilistic and deterministic assessment of seismic soil liquefaction potential. J Geotech Geoenviron Eng 2004;130(12):1314–1340. https://doi.org/10.1061/(ASCE)1090-0241(2004)130:12(1314)

Chandler BMP, Lovell H, Boston CM, Lukas S, Barr ID, Benediktsson ÍÖ, et al. Glacial geomorphological mapping: A review of approaches and frameworks for best practice. Earth Sci Rev 2018;185:806–846. https://doi.org/10.1016/j.earscirev.2018.07.015

Chiaradonna A, Tropeano G, d'Onofrio A, Silvestri F. Development of a simplified model for pore water pressure build-up induced by cyclic loading. Bull Earthq Eng 2018;16(9):3627–3652. https://doi.org/10.1007/s10518-018-0354-4

Chiaradonna A, d'Onofrio A, Bilotta E. Assessment of post-liquefaction consolidation settlement. Bull Earthq Eng 2019;17:Article 695. https://doi.org/10.1007/s10518-019-00695-0.

Chiou, B. S.-J., & Youngs, R. R. Update of the Chiou and Youngs NGA Model for the Average Horizontal Component of Peak Ground Motion and Response Spectra. Earthquake Spectra 2014;30(3):1117–1153. https://doi.org/10.1193/072813EQS219M

D'Apuzzo M, Evangelisti A, Modoni G, Spacagna R-L, Paolella L, Santilli D, et al. Simplified approach for liquefaction risk assessment of transportation systems: Preliminary outcomes. In:

Proceedings of the International Conference on Computational Science and Its Applications, Cagliari, Italy, 1–4 July 2020; 2020. p. 130–45.

Dafalias YF, Manzari MT. Simple plasticity sand model accounting for fabric change effects. J Eng Mech 2004;130(6):622–634.

Earthquake Engineering Research Institute. Loma Prieta Reconnaissance Report. Earthq Spectra 1990;6(Suppl):97–283.

Earthquake Engineering Research Institute. Northridge Earthquake Reconnaissance Report, Vol. 1. Earthq Spectra 1995;11(Suppl C):239.

Earthquake Engineering Research Institute. The Kyogo-Ken Nanbu Earthquake – January 17, 1995 – Preliminary Reconnaissance Report. EERI, Oakland, California; 1995. p. 1, 72.

Ecemiş N. Experimental and numerical modeling on the liquefaction potential and ground settlement of silt-interlayered stratified sands. Soil Dyn Earthq Eng 2021;144(10):106691. https://doi.org/10.1016/j.soildyn.2021.106691

FEMA. Hazus Earthquake Model Technical Manual, Hazus 5.1. FEMA US; 2022.

Gehrmann A, Harding C. Geomorphological mapping and spatial analyses of an Upper Weichselian glacitectonic complex based on LiDAR data, Jasmund Peninsula (NE Rügen), Germany. Geosciences 2018;8(6):208. https://doi.org/10.3390/geosciences8060208.

Geyin M, Maurer BW. Fragility functions for liquefaction-induced ground failure. J Geotech Geoenviron Eng 2020;146(12):04020142. https://doi.org/10.1061/(ASCE)GT.1943-5606.0002416

Giardini D, Wössner J, Danciu L. Seismic Hazard Harmonization in Europe (SHARE): Online Data Resource; 2013. https://doi.org/10.12686/SED-00000001-SHARE

Gkiougkis I, Pouliaris C, Pliakas FK, Diamantis I, Kallioras A. Conceptual and Mathematical Modeling of a Coastal Aquifer in Eastern Delta of R. Nestos (N. Greece). Hydrology 2021;8(1):23. https://doi.org/10.3390/hydrology8010023.

H.T. Harvey & Associates. Airport Roadway Project Port of Oakland, Biotic Habitats and Wetlands Report. Prepared for Woodward-Clyde Consultants and the Port of Oakland; 1993.

Helley EJ, Lajoie KR. Flatland deposits of the San Francisco Bay region, California: Their geology and engineering properties, and their importance to comprehensive planning. U.S. Geological Survey Professional Paper 943; 1979. 88 pp.

Horton R, Trump BD, Trump J, Knowles HS, Linkov I, Jones P, et al. Performance metrics for resilience of airport infrastructure. Transp Res Part D-Transp Environ 2025;142:104676. https://doi.org/10.1016/j.trd.2025.104676.

Idriss IM, Boulanger RW. Soil liquefaction during earthquakes. Monograph MNO-12. Earthquake Engineering Research Institute (EERI); 2008.

Ishihara K, Yoshimine M. Evaluation of settlements in sand deposits following liquefaction during earthquakes. Soils Found 1992;32(1):173–188. https://doi.org/10.3208/sandf1972.32.173

Iwasaki T, Tatsuoka F, Tokida K, Yasuda S. A practical method for assessing soil liquefaction potential based on case studies at various sites in Japan. In: Proceedings of the 2nd International Earthquake Microzonation Conference, Washington, DC; 1978. p. 885–896.

Iwasaki T, Tokida K, Tatsuoka F, Watanabe S, Yasuda S, Sato H. Microzonation for soil liquefaction potential using simplified methods. In: Proceedings of the 3rd International Conference on Microzonation, Vol. 3, Seattle, USA; June 28 - July 1, 1982. p. 1319–1330.

Juang CH, Ching J, Wang L, Khoshnevisan S, Ku CS. Simplified procedure for estimation of liquefaction-induced settlement and site-specific probabilistic settlement exceedance curve using cone penetration test (CPT). Can Geotech J 2013;50(10):1055–1066. https://doi.org/10.1139/cgj-2012-0410.

Knudsen KL, Bott J. Geologic and geomorphic evaluation of liquefaction case histories for rapid hazard mapping. Seismol Res Lett 2011;82(2):334–335.

Lajoie KR, Helley EJ. Differentiation of sedimentary deposits for purposes of seismic zonation. U.S. Geological Survey Professional Paper; 1975. p. A39–A51.

Lakkimsetti B, Latha GM. Role of geofoam inclusions on the liquefaction resilience of transportation geostructures. Transp Geotech 2023;41:101041. https://doi.org/10.1016/j.trgeo.2023.101041

Magliulo P, Valente A. GIS-based geomorphological map of the Calore River floodplain near Benevento (Southern Italy) overflooded by the 15th October 2015 event. Water 2020;12(1):148. https://doi.org/10.3390/w12010148.

Maurer BW, Green RA, Taylor ODS. Moving towards an improved index for assessing liquefaction hazard: Lessons from historical data. Soils Found 2015;55(4):778–787. https://doi.org/10.1016/j.sandf.2015.06.010

McKenna G, Argyroudis SA, Winter MG, Mitoulis SA. Multiple hazard fragility analysis for granular highway embankments: Moisture ingress and scour. Transp Geotech 2021;26:100431. https://doi.org/10.1016/j.trgeo.2020.100431.

Meslem A, Iversen H, Iranpour K, Lang D. A computational platform to assess liquefaction-induced loss at critical infrastructures scale. Bull Earthq Eng 2021;19(11):4083-4224. https://doi.org/10.1007/s10518-020-01021-9

Metropolitan Transportation Commission. Adapting to Rising Tides: Transportation Vulnerability and Risk Assessment Pilot Project Briefing Book; 2011. https://mtc.ca.gov/sites/default/files/Rising_Tides_Briefing_Book.pdf

Minarelli L, Amoroso S, Civico R, De Martini PM, Lugli S, Martelli L, et al. Liquefied sites of the 2012 Emilia earthquake: A comprehensive database of the geological and geotechnical features (Quaternary alluvial Po Plain, Italy). Bull Earthq Eng 2022;20:3659–97. https://doi.org/10.1007/s10518-022-01338-7.

Moss RES, Chen G. Comparing liquefaction procedures in the U.S. and China. In: 14th World Conference on Earthquake Engineering, Beijing, China, October 12–17, 2008.

Nisqually Earthquake Clearinghouse Group. The Nisqually Earthquake of 28 February 2001: Preliminary Reconnaissance Report. University of Washington, Seattle, WA; 2001.

Papathanassiou G. LPI-based approach for calibrating the severity of liquefaction-induced failures and for assessing the probability of liquefaction surface evidence. Eng Geol 2008;96(1-2):94–104. https://doi.org/10.1016/j.enggeo.2007.10.005.

Papathanassiou G, Mantovani A, Tarabusi G, Rapti D, Caputo R. Assessment of liquefaction potential for two liquefaction-prone areas considering the May 20, 2012 Emilia (Italy) earthquake. Eng Geol 2015;189:1–16. https://doi.org/10.1016/j.enggeo.2015.02.002.

Papathanassiou G, Ganas A, Valkaniotis S. Recurrent liquefaction-induced failures triggered by 2014 Cephalonia, Greece earthquakes: Spatial distribution and quantitative analysis of liquefaction potential. Eng Geol 2016;200:18–30. https://doi.org/10.1016/j.enggeo.2015.11.011.

Papatheodorou K, Theodoulidis N, Klimis N, Zulfikar C, Vintila D, Cardanet V, et al. Rapid earthquake damage assessment and education to improve earthquake response efficiency and community resilience. Sustainability 2023;15(24):16603. https://doi.org/10.3390/su152416603.

Pitilakis K, Crowley H, Kaynia AM. SYNER-G: Typology definition and fragility functions for physical elements at seismic risk. Geotech Geol Earthq Eng 2014;27:1–28.

Plafker G, Galloway JP. Lessons learned from the Loma Prieta, California, Earthquake of October 17, 1989. USGS Circular 1045; 1989. https://doi.org/10.3133/cir1045

Ramos A, Grima J, Iturrarán-Viveros U, Silva P. Mechanistic-empirical permanent deformation models. Road Materials and Pavement Design 2020;21(8):2321–2345. https://doi.org/10.1016/j.roadmat.2019.07.003

Schiff AJ, editor. Northridge Earthquake – Lifeline Performance and Post-Earthquake Response. Technical Council on Lifeline Earthquake Engineering Monograph No. 8, American Society of Civil Engineers; 1995. p. 227–235.

Seed RB, Riemer M, Dickenson SE. Liquefaction of soils in the 1989 Loma Prieta Earthquake. In: Proceedings of the International Conferences on Recent Advances in Geotechnical Earthquake Engineering and Soil Dynamics, Vol. 9; 1991.

Sonmez H. Modification of the liquefaction potential index and liquefaction susceptibility mapping for a liquefaction-prone area (Inegol, Turkey). Environ Geol 2003;44(7):862–871.

Sotiriadis D, Margaris B, Klimis N, Dokas IM. Seismic Hazard in Greece: A Comparative Study for the Region of East Macedonia and Thrace. GeoHazards 2023;4:239–266. https://doi.org/10.3390/geohazards4030014

Stewart JP, Klimis N, Savvaidis A, Theodoulidis N, Zargli E, Athanasopoulos G, et al. Compilation of a local Vs profile database and its application for inference of Vs30 from geologic- and terrain-based proxies. Bull Seismol Soc Am 2014;104(6):2827–2841. https://doi.org/10.1785/0120130331

Stournaras G. Evolution et Comportement d'un Systeme Aquifer Heterogene. Geologie et Hydrogeology du Delta Nestos (Greece) et de ses Bordures. Doctoral Thesis, University Grenoble, Grenoble, France; 1984.

Taftsoglou M, Valkaniotis S, Papathanassiou G, Karantanellis E. Satellite imagery for rapid detection of liquefaction surface manifestations: The case study of Türkiye–Syria 2023 Earthquakes. Remote Sens 2023;15(17):4190. https://doi.org/10.3390/rs15174190.

Taftsoglou M, Valkaniotis S, Papathanassiou G, Klimis N, Dokas I. A detailed liquefaction susceptibility map of Nestos River Delta, Thrace, Greece based on surficial geology and geomorphology. Geosciences 2022;12(10):361. https://doi.org/10.3390/geosciences12100361.

Tan Y-Q, Fu Y-K, Li Y-L, Zhang C. Responses of snow-melting airfield rigid pavement under aircraft loads, temperature loads, and their coupling effects. Transportation Geotechnics 2018;14:107–116. https://doi.org/10.1016/j.trgeo.2017.11.006

Tang A, Kwasinski A, Eidinger J, Foster C, Anderson P. Telecommunication systems' performance: Christchurch earthquakes. Earthq Spectra 2014;30(1):231–252. https://doi.org/10.1193/022213EQS046M

Toprak S, Holzer TL. Liquefaction Potential Index: Field assessment. J Geotech Geoenviron Eng 2003;129(4):315–322. https://doi.org/10.1061/(ASCE)1090-0241(2003)129:4(315).

Toyota H, Takada S. Settlement assessment of sand subjected to cyclic stress related to a load moving over a surface using hollow-cylindrical torsional shear apparatus. Transport Geotechnics 2021;29:100580. https://doi.org/10.1016/j.trgeo.2021.100580

Trump BD, Mitoulis S, Argyroudis S, Kiker G, Palma-Oliveira J, Horton R, et al. Threat-agnostic resilience: Framing and applications. Int J Disaster Risk Reduct 2025; 124:105535. https://doi.org/10.1016/j.ijdrr.2025.105535

United States Environmental Protection Agency. Constructed Wetlands for Wastewater Treatment and Wildlife Habitat: 17 Case Studies. EPA 832-R-93-005. Office of Wastewater Management, Washington, DC; September 1993.

Vallerga BA, Grogan WP. A case study: Damage to the Metropolitan Oakland International Airport caused by the Loma Prieta Earthquake. Final Report, Washington, DC; 1992.

van Ballegooy S, Malan P, Jacka ME, Lacrosse V, Leeves JR, Lyth JE. Methods for characterizing effects of liquefaction in terms of damage severity. In: 15th World Conference on Earthquake Engineering, Lisbon, Portugal; 2012.

van Ballegooy S, Malan P, Lacrosse V, Jacka M, Cubrinovski M, Bray J, et al. Assessment of liquefaction-induced land damage for residential Christchurch. Earthq Spectra 2014;30(1):31–55. https://doi.org/10.1193/031813EQS070M.

Wakamatsu K. Evaluation of liquefaction susceptibility based on detailed geomorphological classification. In: Proceedings of the Annual Meeting of Architectural Institute of Japan; 1992. p. 1443–1444.

Washington Division of Geology and Earth Resources. Surface geology, 1:100,000—GIS data. Digital Data Series DS-18, Version 3.1. Originally released June 2010; 2016.

Werner SD, Taylor CE, Cho S, Lavoie J-P, Huyck C, Eitzel C, et al. Redars 2 methodology and software for seismic risk analysis of highway systems. Special Report MCEER-06-SP08. Multidisciplinary Center for Earthquake Engineering Research, University at Buffalo; 2006.

William Lettis & Associates, Inc. Evaluation of earthquake-induced liquefaction hazards at San Francisco Bay Area commercial airports. Report prepared for the Association of Bay Area Governments; 1999. 37 p.

Witter RC, Knudsen KL, Sowers JM, Wentworth CM, Koehler RD, Randolph CE, et al. Maps of Quaternary deposits and liquefaction susceptibility in the central San Francisco Bay region, California. U.S. Geological Survey Open-File Report 2006-1037; 2006. Scale 1:100,000.

Yanites BJ, Clark MK, Roering JJ, West AJ, Zekkos D, Baldwin JW, et al. Cascading land surface hazards as a nexus in the Earth system. Science 2025;388(6754). https://doi.org/10.1126/science.adp9559.

YDRODOMIKI. Economic Feasibility Study of Irrigation in Rhodope-Xanthi-Kavala and Drama Districts by Thisavros-Temenos Dams of Nestos River. Department of Agriculture, Athens, Greece; 1985 (in Greek).

YDROEREUNA. Hydrological Survey of Alluvial Area in Delta of Nestos. YDROEREUNA, Athens, Greece; 1978 (in Greek).

Youd TL, Hoose SN. Historic ground failures in Northern California triggered by earthquakes. U.S. Geological Survey Professional Paper 993; 1978. https://doi.org/10.3133/pp993

Youd TL, Perkins DM. Mapping of liquefaction-induced ground failure potential. J Geotech Eng Div 1978;104(4):433–446. https://doi.org/10.1061/AJGEB6.0000612

Youd TL, Idriss IM, Andrus RD, Arango I, Castro G, Christian JT, Dobry R, Finn WDL, et al. Liquefaction resistance of soils: Summary report from the 1996 NCEER and 1998 NCEER/NSF workshops. J Geotech Geoenviron Eng 2001;127:297-313. http://dx.doi.org/10.1061/(ASCE)1090-0241(2001)127:4(297)

Zalachoris, G., Zekkos, D., Athanasopoulos-Zekkos, A., Gerolymos, N. (2021). The role of liquefaction on the seismic response of quay walls during the 2014 Cephalonia, Greece, earthquakes. Journal of Geotechnical and Geoenvironmental Engineering, 147(12), 04021137.

Zhang G, Robertson PK, Brachman RWI. Estimating liquefaction-induced ground settlements from CPT for level ground. Can Geotech J 2002;39(5):1168–1180. https://doi.org/10.1139/t02-047

Zhang Y, Xue D, Zhou S, Zhang M, Wen H. Simulation analysis of the effects of liquefaction on pile foundations under seismic response. In: Feng G, Editor. Proc. of the 10th International Conference on Civil Engineering. ICCE 2023. Lecture Notes in Civil Engineering, 526. Springer, Singapore; 2024. https://doi.org/10.1007/978-981-97-4355-1_17.

Zhu J, Daley D, Baise LG, Thompson EM, Wald DJ, Knudsen KL. A Geospatial Liquefaction Model for Rapid Response and Loss Estimation. Earthquake Spectra. 2015; 31(3): 181–200. Springer, USA. https://doi.org/10.1193/121912EQS353M.

Declaration of interests

☒ The authors declare that they have no known competing financial interests or personal relationships that could have appeared to influence the work reported in this paper.

☐ The authors declare the following financial interests/personal relationships which may be considered as potential competing interests: